Natural Resources Canada   Ressources naturelles Canada

GEOMATICS CANADA
OPEN FILE 63

The Government of Canada automated processing system for change detection and ground deformation analysis from RADARSAT-2 and RADARSAT Constellation Mission Synthetic Aperture Radar data: description and user guide

J.P. Dudley and S.V. Samsonov

2020

Canada

GEOMATICS CANADA
OPEN FILE 63

The Government of Canada automated processing system for change detection and ground deformation analysis from RADARSAT-2 and RADARSAT Constellation Mission Synthetic Aperture Radar data: description and user guide

J.P. Dudley and S.V. Samsonov

2020

Permanent link: https://doi.org/10.4095/327790

This publication is available for free download through GEOSCAN (https://geoscan.nrcan.gc.ca/).

Recommended citation
Dudley J.P. and Samsonov S.V., 2020. The Government of Canada automated processing system for change detection and ground deformation analysis from RADARSAT-2 and RADARSAT Constellation Mission Synthetic Aperture Radar data: description and user guide; Geomatics Canada, Open File 63, 65 p. https://doi.org/10.4095/327790

Publications in this series have not been edited; they are released as submitted by the author.

Contents

1. Introduction 2
2. Synthetic Aperture Radar processing techniques 2
2.1 Differential Interferometric Synthetic Aperture Radar (DInSAR) 4
2.1.1 Quality control of DInSAR – coherence and baselines 6
2.2 Speckle Offset-tracking (SPO) 6
2.2.1 Quality control of SPO – signal-to-noise ratio 7
2.3 Digital Elevation Model 7
2.4 Time series 8
2.4.1 DInSAR 8
2.4.2 SPO range and azimuth 9
2.4.3 SPO 3D 9
3. Applications and recommended processing techniques 9
4. Processing manual 10
4.1 SAR data 10
4.2 RADARSAT-2 data options 10
4.3 RCM data options 11
4.3.1 Submitting an OHS request 13
4.4 Submitting an EODMS request 13
4.5 DInSAR Products 14
5. Examples 15
5.1 DInSAR 15
5.2 SPO 24
6. Conclusion 34
6.1 Future work 35
6.2 Feedback address 35
6.3 Acknowledgements 35
7. References 36
Appendix A: EODMS DInSAR Tutorial 39
Appendix B: Filename Acronyms 65

1. Introduction

The Canada Centre for Mapping and Earth Observation (CCMEO) has developed an automated system for generating standard and advanced deformation products and change detection from Synthetic Aperture Radar (SAR) data acquired by RADARSAT-2 and RADARSAT Constellation Mission (RCM) satellites using Differential Interferometric Synthetic Aperture Radar (DInSAR[1]) processing methodology. This system is designed for, and can only be accessed by, Government of Canada employees. Background information on DInSAR processing and interpretation can be found in the following publications (in order of relevance) and is briefly summarized in the following sections:

- (Ferretti et al., 2007) part A - guidelines for InSAR processing and interpretation;
- (Bamler and Hartl, 1998; Massonnet and Feigl, 1998; Hooper et al., 2012) – DInSAR review papers;
- (Berardino et al., 2002; Lanari et al., 2004; Samsonov et al., 2011)– SBAS-DInSAR;
- (Strozzi et al., 2007) – offset-tracking;
- (Bechor and Zebker, 2006)– multi-aperture interferometry (MAI);
- (Ferretti et al., 2007) part B – practical approach to InSAR processing;
- (Ferretti et al., 2007) part C – mathematical approach to InSAR processing.

This document is intended to act as a guide for new users. The first three sections introduce the processing techniques employed by the system along with their respective quality control measures. Following this, a variety of applications which are appropriate for these processing techniques are presented. The appropriate conditions and ground movement types for each technique are reviewed.

The fourth section provides a processing manual for users. The details of SAR data are introduced, including characteristics such as polarization, resolution, coverage, beam modes, incidence angle and other considerations. The data options offered by RADARSAT-2 and RCM are presented. Methods for acquiring SAR data as well as processing this data are summarized along with a link to a more complete tutorial in Appendix A at the end of the document. An explanation of the products this processing offers is also given.

Following this, examples of each processing technique are presented. These examples help to provide context for when each technique is appropriate as well as to indicate what the expected results can provide as measurements of ground movement.

The document concludes with a discussion of future work.

2. Synthetic Aperture Radar processing techniques

Imaging radar illuminates an area on the ground to create a two-dimensional (2D) image. The radar system generates microwave signals (pulses) that are emitted by the antenna and then measures

[1] Note that InSAR and DInSAR abbreviations are frequently used interchangeably

the portion of the signals reflected back (backscattered) from the area of interest (footprint) using a specialized receiver system (Figure 1). By measuring the time delay between the signal transmission and reception of the backscatter (radar echoes) from different targets, their distance from the radar and thus their locations can be determined. As the radar moves from point A to point B along the satellite flight path, it transmits a pulse at each position within a range of incident angles away from nadir. The return echoes pass through the receiver, are recorded, and a series of signal processing steps permit generation of a radar product of the illuminated area or swath.

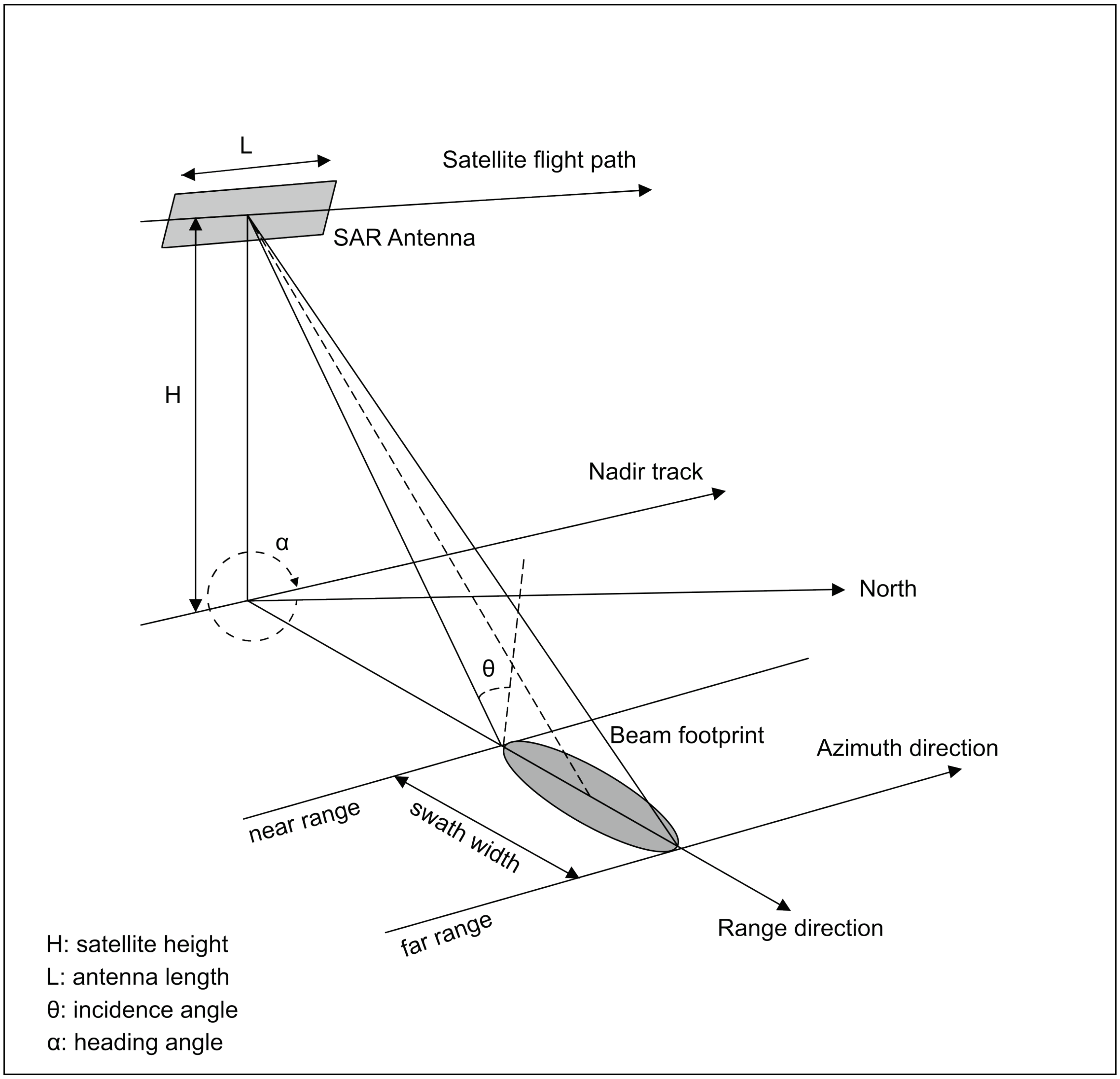

Figure 1: The SAR technique used to synthesize a very long antenna by combining signals (echoes) received by the radar as it moves along its flight track. A synthetic aperture is constructed by moving a real aperture or antenna through a series of positions along the flight track.

In SAR data, range refers to the cross-track dimension perpendicular to the flight direction while azimuth refers to the along-track dimension parallel to the satellite flight direction. The edge of the swath closest to the nadir track is known as the near range while its other edge is known as the far range. Between the near and far range, the radar antenna measures the line-of-sight (LOS) distance between the radar and each target on the surface.

The radar spatial resolution is a function of both the viewing geometry and the microwave signal properties. In addition, the range resolution depends on the duration of the pulse. This means that high range resolution can be achieved by using a shorter pulse length. The azimuthal resolution, known also as the cross-range resolution, depends on the angular width of the transmitted microwave signal and slant range distance. Since radar bandwidth is inversely proportional to the length of the radar antenna, finer azimuthal resolution requires a longer radar antenna. The SAR technique is used to synthesize a very long antenna by combining signals (echoes) received by the radar as it moves along its flight track. A synthetic aperture is constructed by moving a real aperture or antenna through a series of positions along a flight track (Houghton, 1989).

Moreover, because the radar moves relative to the ground, the returned echoes are Doppler-shifted: negatively as the radar approaches a target; positively as it moves away. Comparing the Doppler-shifted frequencies to a reference frequency allows many returned signals to be focused on a single point, effectively increasing the length of the antenna that is imaging that particular point. This focusing operation, commonly known as SAR processing, is now done digitally on fast computer systems. SAR processing algorithms match the variation in Doppler frequency for each point in the image using precise knowledge of the relative motion between the platform and the imaged objects, which is the cause of the Doppler variation in the first place.

2.1 Differential Interferometric Synthetic Aperture Radar (DInSAR)

DInSAR is a powerful technique for generating ground deformation products by combining two or more SAR acquisitions. The phase of a single SAR acquisition is of no practical use due to its ambiguity. However, the phase difference between two SAR acquisitions, $A_1 = A_0 e^{-i\varphi_1}$ and $A_2 = A_0 e^{-i\varphi_2}$, can be exploited for measuring ground deformation. Here A_1 and A_2 represent Single Look Complex (SLC) SAR data with amplitude A_0 and phases φ_1 and φ_2. Two SAR acquisitions can be acquired simultaneously if two SAR antennas are mounted on the same platform (e.g. the Shuttle Radar Topographic Mission), or acquired at different times using repeat orbits of the same satellite (e.g. RADARSAT-2 and RCM). Consecutive radar acquisitions are separated in the time domain, known as temporal baseline and may be separated in the spatial domain, known as spatial (specifically, perpendicular) baseline. Usually the quality of DInSAR products is higher when both temporal and perpendicular baselines ($B_\perp$) are small, but seasonal effects may also affect the quality. Ground deformation is measured along the radar LOS.

The phase difference ($\Delta\varphi$) image or interferogram is the product of one complex SAR image (master) and the complex conjugate of another SAR image (dependent) after the dependent is co-registered to the master projection with sub-pixel precision. The phase difference receives various contributions, such as from the Earth's curvature ($\Delta\varphi_{flat}$), the topography ($\Delta\varphi_{topo}$), ground deformation occurring between the observations ($\Delta\varphi_{def}$), and the sum of other various sources of noise including atmospheric effects ($\Delta\varphi_{noise}$). Therefore, the observed phase difference $\Delta\varphi$ can be expressed as:

$$\Delta\varphi = \Delta\varphi_{flat} + \Delta\varphi_{topo} + \Delta\varphi_{def} + \Delta\varphi_{noise}$$

The $\Delta\varphi_{flat}$ component due to the Earth's curvature can be removed using an interferogram flattening process. The $\Delta\varphi_{topo}$ component depends on both ground height and the perpendicular baseline at the target pixel (Hanssen, 2002), it can be computed using an available Digital Elevation Model (DEM). The presence of possible errors in the DEM can introduce additional phase noise.

The $\Delta\varphi_{noise}$ component accounts for noise from various sources. One source of phase noise is due to the difference in atmospheric conditions at the time of SAR acquisitions. Atmospheric turbulence causes differences in SAR propagation path lengths. Temporal variability of the atmosphere degrades the precision of interferometric phase that can reach tens of centimeters (Zebker and Villasenor, 1992). Tropospheric phase delay is mostly attributed to the spatial and temporal variability of atmospheric water vapor, resulting in spatial fringes that can also be highly correlated with topography. Moreover, the degree of ionospheric phase delay changes between night and daytime. The ionospheric delay is inversely proportional to the square of the frequency, meaning that shorter wavelengths are less susceptible to the ionospheric effect (Jehle et al., 2010). Existing techniques to correct atmospheric contributions include the incorporation of external data provided by meteorological stations, optical remote sensing products such as MODIS and MERIS (Li et al., 2005, 2006), and statistical analysis (Samsonov et al., 2014).
In order to produce a deformation map, phase filtering to reduce noise and unwrapping are required.

Phase unwrapping is the process of adding the correct multiple of 2π to the interferometric fringes to recover the absolute phase difference ($\Delta\varphi_{def}$), since the interferometric phase is wrapped modulo 2π. The process of unwrapping the phase assumes that the deformation pattern is relatively smooth such that the phase differences are less than 2π between two adjacent pixels. This is a critical threshold, which also presents a limitation for DInSAR. Theoretically, the maximum deformation that is measured efficiently with SAR data can be modeled with the wavelength of the radar signals and pixel sizes (e.g. Jiang et al., 2011). For sites with steep deformation gradients one may need to pursue alternative methods, such as offset tracking, to derive reliable deformation measurements from SAR information (Yun et al., 2007).

DInSAR captures ground movement through a one-dimensional LOS measurement. However, ground movement generally occurs in three-dimensional space (east/west, north/south, up/down). This three-dimensional movement is projected into the sensor's LOS through its imaging geometry. This geometry is defined by an incidence angle θ (angle between the beam and the local surface normal), and a heading angle α (angle drawn from north to the direction of the satellite movement, 0-360°). The incidence angle can depend upon the beam mode and can vary between shallow angles (~55°) to steeper angles (~15°). Orbital SAR sensors operate in nearly polar orbits so the heading angle is generally close to 350° (NNW) for ascending passes and 190° (SSW) for descending passes. For constant geometry, the LOS measurement (d_{los}) is expressed as:

$$d_{los} = \sin\alpha \sin\theta d_{north} - \cos\alpha \sin\theta d_{east} + \cos\theta d_{vertical}$$

Due to the generally small value of $\sin\alpha$ (~0.2), DInSAR is less sensitive to ground movement in the north/south direction when compared with equivalent movement in the east/west or vertical directions. In reality, the incidence and heading angles can vary across the scene. The relationship for this variable geometry is presented in Section 2.3.

2.1.1 Quality control of DInSAR – coherence and baselines

The quality of an interferogram, and hence the reliability of derived ground deformation products, is affected by spatial and temporal decorrelation between the two SAR acquisitions (Zebker and Villasenor, 1992; Ferretti et al., 2001). Temporal decorrelation may be caused by ground surface change (e.g. vegetation change, ice or snowmelt, soil moisture change, etc.) and the spatial decorrelation may include Doppler centroid and imaging geometry differences between the two acquisitions. Orbital maintenance has been a concern in past, because satellite drift can result in pairs with large perpendicular baselines which have lower coherence or may be unsuitable for interferometry altogether (RADARSAT-1 for example). This however, has become less of an issue as the importance of precise orbit maintenance is understood and practiced by RCM.

The amount of decorrelation is quantified by estimating interferometric coherence, which is the cross-correlation of the SAR data pair estimated over a local window

$$\rho = |A| = \frac{|A_1 A_2^*|}{\sqrt{A_1 A_!^*}\sqrt{A_2 A_2^*}}$$

where ρ is the coherence, which ranges from 0 to 1, with coherence values approaching 1 indicating reliable signals. Therefore, coherence can be used to select areas where the phase information can be used meaningfully. The size of the window is a trade-off between the spatial resolution and an unbiased estimation of the coherence. Small windows ensure high spatial resolution but with likelihood of biased coherence estimation toward higher values (Touzi et al., 1999), whereas large windows may underestimate coherence in heterogeneous surfaces. In this case, the presence of a large scale deformation gradient may reduce the calculated spatial coherence.

Coherence products are also useful information sources in themselves, providing information about where change has occurred even if that change is not quantifiable.

2.2 Speckle Offset-tracking (SPO)

Amplitude components of SAR data can be used to measure large local deformation with a subpixel tracking method (e.g. Michel and Avouac, 1999). This approach requires the same repeat pass interferometric SAR data sets as DInSAR and tracks the relative displacement of small image chips by applying a 2-dimensional cross-correlation algorithm to the co-registered SAR image pairs (Gray et al., 2001; Short and Gray, 2004, 2005; Van Wychen et al., 2012).

This technique can achieve an accuracy better than 1/20th of the pixel size in the slant range and azimuth directions (Strozzi et al., 2002) but this accuracy is still much less than the accuracy of 1-2 cm provided with DInSAR (Fialko et al., 2001). Since the measurement of a sub-pixel map is scaled within one pixel, the ability of the method can also vary with the real pixel size (Singleton et al., 2014). Therefore, a pair of SAR data with a spatial resolution of 1 m can provide more precise results than a pair of SAR data with a spatial resolution of 30 m. The method has the great advantage of measuring deformation in both azimuth and range directions with a single pair. By combining the 2-dimensional deformation result with a third data source, or making assumptions about local slopes and flow directions, offset-tracking results can be used to derive 3-dimensional deformation measurements.

As with DInSAR, the one-dimensional range and azimuth offsets can be expressed in terms of their three-dimensional components in a constant geometry. For the range offsets, the relationship is identical to that of DInSAR:

$$d_{range} = \sin\alpha \sin\theta d_{north} - \cos\alpha \sin\theta d_{east} + \cos\theta d_{vertical}$$

For the azimuth offsets the relationship is:

$$d_{azimuth} = \cos\alpha\, d_{north} + \sin\alpha\, d_{east}$$

The relationships for a variable geometry are presented in Section 2.3

2.2.1 Quality control of SPO – signal-to-noise ratio

Unlike DInSAR, which relies upon the interferometric coherence between images, SPO quality is determined through the signal-to-noise ratio of the cross correlation function. The peak of the cross-correlation function is compared against regions within a window centered upon the peak. This ratio determines the quality of the cross correlation and offset measurement. Regions with low signal-to-noise indicate a less reliable measurement. This ratio can be influenced by the cross correlation window size and in turn the size of the expected offsets.

2.3 Digital Elevation Model

A Digital Elevation Model is required for both DInSAR and SPO processing. A DEM is used to coregister and geocode data and also to model the topographic phase in DInSAR processing. The automated system allows a user to select between three DEMs, listed in Table 1.

Table 1: Digital Elevation Models

DEM	Resolution (m)	Coverage
Canadian Digital Elevation Model (CDEM)	30	All of Canada
Canadian Digital Surface Model (CDSM)	20	Canada south of 60°N
Shuttle Radar Topographic Mission (SRTM) - Canada	30	Canada south of 60°N
Shuttle Radar Topographic Mission (SRTM) - World	90	World between 60°S and 60°N

The CDEM covers all regions in Canada with a resolution of 30 meters. The CDSM incorporates the SRTM digital surface model (DSM) to increase resolution to 20 meters, however it only covers regions in Canada south of latitude 60°N. The SRTM Canada has a resolution of 30 meters and covers Canada south of latitude 60°N. The SRTM World has a resolution of 90 meters and covers the world between latitudes 60°S and 60°N.

Additional global DEM coverage can be provided with the Advanced Spaceborne Thermal Emission and Reflection Radiometer (ASTER) 90 meter DEM. This DEM can be incorporated into the system if there is sufficient demand.

The DEM also allows for the calculation of the look vectors. These vectors are oriented from the targets towards the sensor and are defined through the elevation (Θ_{LV}) and orientation (Φ_{LV}) look vector angles. The filenames for these vectors end in *lv_theta.geo.tif* and *lv_phi.geo.tif*. Unlike the constant geometry discussed in Sections 2.1 and 2.2 , these angles can vary across the scene. In order to calculate the range and azimuth offsets, the look vectors and displacements must be calculated at each pixel position in the scene. In general, this is calculated either with a loop over all pixels or via matrix multiplication.

For DInSAR and the SPO range offsets, the relationship between the LOS measurement and the look vector is:

$$d_{los} = \sin \Phi_{LV} \cos \Theta_{LV} d_{north} + \cos \Phi_{LV} \sin \Theta_{LV} d_{east} + \sin \Theta_{LV} d_{vertical}$$

For the SPO azimuth offsets, the relationship is:

$$d_{los} = - \cos \Phi_{LV} d_{north} + \sin \Phi_{LV} d_{east}$$

2.4 Time series

Time series or multi-temporal analysis of DInSAR and SPO measurements uses many, often overlapping measurements of discrete time periods to monitor ground deformation over an extended period. A linear deformation rate can also be calculated over the measurement period.

2.4.1 DInSAR

The multi-temporal DInSAR processing is based upon the Multidimensional Small Baseline Subset (MSBAS) (Samsonov and d'Oreye, 2012; Berardino et al., 2002; Lanari et al., 2004; Samsonov et al., 2011) technique. This method employs Singular Value Decomposition (SVD) processing of highly coherent interferograms, usually acquired with small temporal and perpendicular baselines. These methods are capable of generating non-linear time-series of ground deformation. When required, temporal interpolation and regularization are used to create a continuous measurement set. For DInSAR, all measurements are made in the line-of-sight of the beam mode (defined by incidence and heading angles).

2.4.2 SPO range and azimuth

For SPO processing, the MSBAS technique is also employed. In this case, measurements are made along the range and azimuth directions. These directions are defined by the satellite track (azimuth) and the direction perpendicular to it (range).

2.4.3 SPO 3D

SPO measurement made along the range and azimuth directions can be rotated into measurement along the cardinal directions (east/west, north/south, up/down) by including an additional constraint to the movement. This additional constraint requires the ground movement to follow local topographic gradients (surface parallel flow) and is only applicable in cases where the ground movement is expected to move along slopes (e.g. glacial flow). In this case, MSBAS techniques are employed and cumulative ground movement is expressed in the north/south, east/west, and up/down directions.

3. Applications and recommended processing techniques

Deformation and change detection products produced with DInSAR can be used in a variety of applications, some of which are listed in Table 2. Each application is characterized by its temporal duration, relative to the RCM orbit revisit cycle of four days, and magnitude of displacement, relative to the RCM wavelength of 5.55 cm. For example, abrupt duration means that events occur almost instantaneously (e.g. earthquake), while gradual duration means that events occur over a period longer than four days (e.g. mining induced subsidence). Small magnitude means displacement smaller than satellite wavelength of 5.55 cm (e.g. inter-seismic motion), while very large magnitude means displacements larger than a few 10s of cm (e.g. earthquake).

Table 2: Supported applications

Applications	Duration	Displacement Magnitude
Earthquakes	Abrupt	Small to very large
Volcanoes	Gradual and abrupt	Small to very large
Landslides	Gradual and abrupt	Small to very large
Tectonics	Gradual	Predominantly small
Permafrost	Gradual	Predominantly small
Glacial motion	Gradual	Predominantly very large
Anthropogenic (mining, groundwater, carbon capture and storage-CCS)	Gradual and abrupt	Predominantly small to large
Change detection	Gradual and abrupt	N/A, detects coherence loss only

The following Table 3 lists recommended products for each application.

Table 3: Applications and recommended products.

Applications/Recommended Products	DInSAR	MSBAS-DInSAR	SPO	MSBAS-SPO	RMLI	Coherence
Earthquakes (co-seismic)	☑		☑			
Volcanoes	☑	☑				
Landslides	☑	☑				
Tectonics	☑	☑				
Permafrost		☑				
Glacial motion	☑		☑	☑		
Anthropogenic (mining, groundwater, CCS)	☑	☑				
Change detection					☑	☑

4. Processing manual

This section will describe the input and output data use in the DInSAR and SPO processing techniques. Input SAR data will be detailed for the RADARSAT-2 and RCM sensors. The available SLC beam modes along with their respective beam properties will be listed. Output DInSAR products and descriptions will also be presented.

4.1 SAR data

Conventional DInSAR processing requires two or more single look complex (SLC) products acquired with identical SAR characteristics (wavelength, beam mode and polarization) and virtually identical imaging geometry, essentially limiting DInSAR to repeat pass acquisitions of the same satellite or single track acquisitions from multiple but identical satellites. High resolution and co-polarization (HH or VV) modes are more suitable as they deliver higher interferometric coherence.

For performing DInSAR analysis, it is important to consider what would be suitable data in terms of resolution and wavelength for the application (Massonnet and Feigl, 1998). Another issue is related to the quality of the DEM used to remove topographic phase contributions from the interferograms. This is particularly critical for mapping spatially small deformation and a high resolution DEM ensures higher accuracy DInSAR products.

4.2 RADARSAT-2 data options

RADARSAT-2 is a C-band (5.55 cm wavelength) satellite orbiting at 798 km altitude. The orbit revisit cycle the satellite is 24 days. RADARSAT-2 data can be acquired in several beam modes with varying spatial resolution, coverage, polarization and noise floor characteristics, as listed in Table 4[2]. The list of possible polarizations for SLC data includes:

- Single (HH, HV, VH, VV);
- Dual (HH+HV, VV+VH), HH+VV is available only for Ship detection, Low noise, and Spotlight beam modes;
- Quad (HH+VV+HV+VH);

Table 4: RADARSAT-2 beam modes suitable for DInSAR analysis, where L is the slant range and azimuth spatial sampling, θ is the nominal incidence angle range, R and A are multi-looking numbers in range and azimuth respectively, and NESZ is the nominal Noise Equivalent Sigma Zero that describes the sensitivity of the SAR system.

Beam Name	Beam Type	Resolution (m)	Swath (km)	Looks (R x A)	L (m)	θ°	NESZ (dB)
Extended High	Stripmap	13.5 x 7.7	75 x75	1 x 1	11.8 x 5.1	49-60	-28
Extended Low	Stripmap	9.0 x 7.7	170 x 170	1 x 1	8.0 x 5.1	10-23	-27
Wide	Stripmap	13.5 x 7.7	150 x 150	1 x 1	11.8 x 5.1	20-45	-28
Standard	Stripmap	9.0 x 7.7	100 x 100	1 x 1	8 x 5.1	20-52	-29
Wide Standard Quad-Pol	Stripmap	9.0 x 7.6	50 x 25	1 x 1	8 x 5.1	18-42	-35
Standard Quad-Pol	Stripmap	9.0 x 7.6	25 x25	1 x 1	8 x 5.1	18-49	-38
Wide Fine	Stripmap	5.2 x 7.7	150 x 150	1 x 1	4.7 x 5.1	20-45	-24
Fine	Stripmap	5.2 x 7.7	50 x50	1 x 1	4.7 x 5.1	30-50	-26
Wide Fine Quad-Pol	Stripmap	5.2 x 7.6	50 x 25	1 x 1	4.7 x 5.1	18-42	-33
Fine Quad-Pol	Stripmap	5.2 x 7.6	25 x 25	1 x 1	4.7 x 5.1	18-49	-35
Extra-Fine	Stripmap	3.1 x 4.6	125 x 125	1 x 1	2.7 x 2.9	22-49	-21
Wide Multi-Look Fine	Stripmap	3.1 x 4.6	90 x 50	1 x 1	2.7 x 2.9	29-50	-19
Multi-Look Fine	Stripmap	3.1 x 4.6	50 x 50	1 x 1	2.7 x 2.9	30-50	-20
Wide Ultra-Fine	Stripmap	1.6 x 2.8	50 x 50	1 x 1	1.3 x 2.1	29-50	-22
Ultra-Fine	Stripmap	1.6 x 2.8	20 x 20	1 x 1	1.3 x 2.1	20-54	-26.5
Spotlight	Spotlight	1.6 x 0.8	18 x 8	1 x 1	1.3 x 0.4	20-54	-28.5

4.3 RCM data options

The RCM consists of three C-band (5.55 cm wavelength) satellites orbiting at 592.7 km altitude. The orbit revisit cycle of each individual satellite is twelve days and the orbit revisit cycle of the constellation is four days. The four days DInSAR potential strengthens operational use of SAR data in applications that require continuous collection of data. The RCM data can be acquired in several beam modes with varying spatial resolution, coverage, polarization and noise floor characteristics, as listed in Table 5[3] and presented in Figure 2. The list of possible polarizations for SLC data includes:

- Single (HH, HV, VH, VV);

[2] A full product description for RADARSAT-2 can be found at https://mdacorporation.com/docs/default-source/technical-documents/geospatial-services/52-1238_rs2_product_description.pdf
[3] Technical characteristics of RCM can be found at https://www.asc-csa.gc.ca/eng/satellites/radarsat/technical-features/characteristics.asp

- Dual (HH+HV, VV+VH), HH+VV is available only for Ship detection, Low noise, and Spotlight beam modes;
- Quad (HH+VV+HV+VH);
- Compact (CH+CV);

Table 5: RCM beam modes suitable for DInSAR analysis, where L is the slant range and azimuth spatial sampling, θ is the nominal incidence angle range, R and A are multi-looking numbers in range and azimuth respectively, and NESZ is the nominal Noise Equivalent Sigma Zero that describes the sensitivity of the SAR system.

Beam Name	Beam Type	Resolution (m)	Swath (km)	Looks (R x A)	L (m)	θ°	NESZ (dB)
Ship Detection	ScanSAR	variable	350	5 x 1	1.4 x 34.4	40-58	variable
Low Noise	ScanSAR	100	350	4 x 2	8.7 x 69.1	19-58	-25
Low Resolution 100m	ScanSAR	100	500	8 x 1	4.2 x 69.1	19-54	-22
Medium Resolution 50m	ScanSAR	50	350	4 x 1	4.2 x 34.5	19-58	-22
Medium Resolution 30m	ScanSAR	30	125	2 x 2	4.2 x 23.0	19-47	-24
Medium Resolution 16m	Stripmap	16	30	1 x 4	6.3 x 2.2	19-47	-25
Quad-Polarization	Stripmap	9	20	1 x 1	3.1 x 2.9	29-44	-24
High Resolution 5m	Stripmap	5	30	1 x 1	2.1 x 2.2	19-54	-19
Very High Resolution 3m	Stripmap	3	20	1 x1	1.4 x 1.9	19-54	-17
Spotlight	Spotlight	3 x 1	20 x 5	1 x 1	1.4 x 0.5	19-47	-17

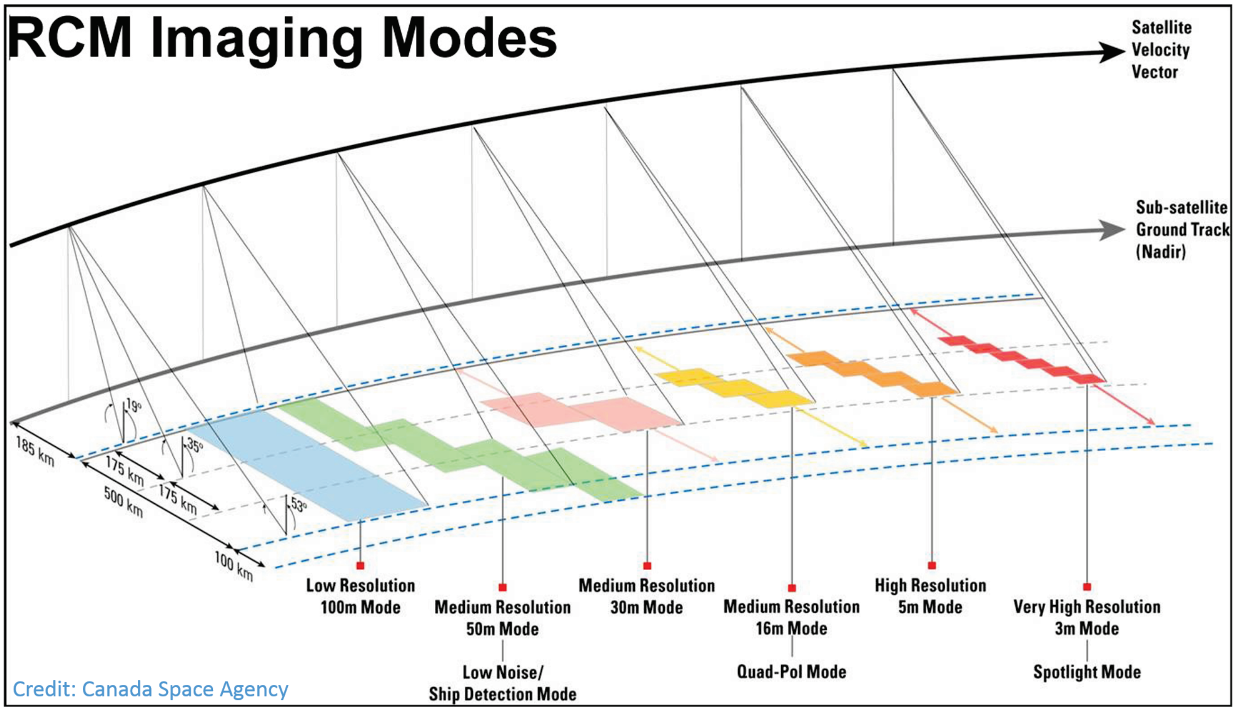

Figure 2: Imaging modes of the RADARSAT Constellation Mission.

4.3.1 Submitting an OHS request

To program and acquire new RCM SAR imagery, the user must access the RCM Order Handling System (OHS). The OHS can only be accessed by vetted Government of Canada employees This system allows a user to submit a request for new image acquisitions over a particular area of interest. Beam mode characteristics (resolution, polarization, look-up table) can all be defined by the user. An assessment tool is provided to ascertain the likelihood of successful image acquisition, given the priority of the data request and the available SAR on-time of the satellites.

4.4 Submitting an EODMS request

To generate DInSAR products using the automated DInSAR processing system, the user needs to access the Value Added Product (VAP) toolbox within the Earth Observation Data Management System (EODMS). EODMS is open to the public, however the VAP toolbox can only be accessed by vetted Government of Canada users. Through the VAP interface, users can select input data and specific processing parameters. A complete, step-by-step tutorial on how to access the system, locate catalog data, and create a DInSAR processing request is presented in Appendix A.

Once a processing request has been created, it is translated into an XML file and transferred, along with the SAR data and appropriate DEM segment, to a High Performance Computing cluster (HPC) where the DInSAR processing system is hosted, and placed in the Inbox.

Once the DInSAR processing is completed, results are picked up from the Outbox (transfer is initiated by the EODMS VAP toolbox) and transferred back to EODMS where they can be accessed by the user. The interactions between EODMS and the automated DInSAR processing system are performed using SSH protocol. The automated DInSAR system uses a queue protocol and orders are processed as computing resources become available. The life cycle for each job is set to 24 hours with a total disk capacity of 180TB. The processing system is based on the commercial Gamma Remote Sensing processing software (GAMMA) and an ensemble of automated scripts using the Bash, Python and C languages. The interface of EODMS has several tabs to facilitate the building of a processing request by the user. Registration is required for using the EODMS and VAP system.

4.5 DInSAR Products

A list of DInSAR products is presented in Table 6. All output data products will be geocoded and delivered in GeoTIFF, kmz, and PDF formats. All GeoTIFF products have a 4 byte float format and are in the WGS84 projection.

Table 6: Supported products

Product	Abbreviation	Description	Unit
Digital Elevation Model	DEM	Digital Elevation Model extracted from the source specified through EODMS interface (CDEM, CDSM, SRTM)	m
Coregistered intensity	RMLI	Multi-looked intensity images	
Coherence		Cross-correlation coefficient of the SAR image pair estimated over a small window	
Coherence (filtered)		Coherence after applying adaptive filtering	
Wrapped phase		Differential interferogram of the SAR image pair, flattened and topographic phase removed	rad
Wrapped phase (filtered)		Differential interferogram after applying adaptive filtering	rad
Unwrapped phase		Unwrapped filtered differential interferogram	rad
Range displacement	DInSAR	Ground displacement along the satellite line of sight (LOS)	m
Range displacement time series and rate	MSBAS	Time series of ground displacements for each SLC epoch and linear rate	m, m/yr
Azimuth/range displacement	SPO	Range and azimuth offset maps from speckle offset tracking	m
Azimuth/range displacement time series and rate	MSBAS	Range and azimuth offset displacements for each SLC epoch and linear rate	m, m/yr
3D displacement (surface parallel flow)	SPO	East, north, and vertical offset maps derived from azimuth/range displacement assuming surface parallel flow	m

Product	Abbreviation	Description	Unit
3D displacement time series and rate (surface parallel flow)	MSBAS	East, north, and vertical offset displacements for each SLC epoch and linear rate	m, m/yr

5. Examples

In this section, two case study examples demonstrating two classes of ground deformation will be presented. The first example will focus on a ground deformation process which is appropriate for DInSAR analysis. Here the ground movement is not expected to exceed a few centimeters between the sensor repeat pass interval (4 days for RCM). The second example will focus on much larger ground movement and will employ SPO analysis. In this case, the expected movement is on the order of meters between the sensor repeat pass interval (24 days for RADARSAT-2).

5.1 DInSAR

The Thompson River valley is an important transportation corridor in British Columbia which is known to have landslide activity. By using DInSAR techniques with high resolution RCM data, this region can be monitored for ground movement every 4 days. The region of interest is presented in both Google Earth optical imagery and an RMLI image from RCM in Figure 3.

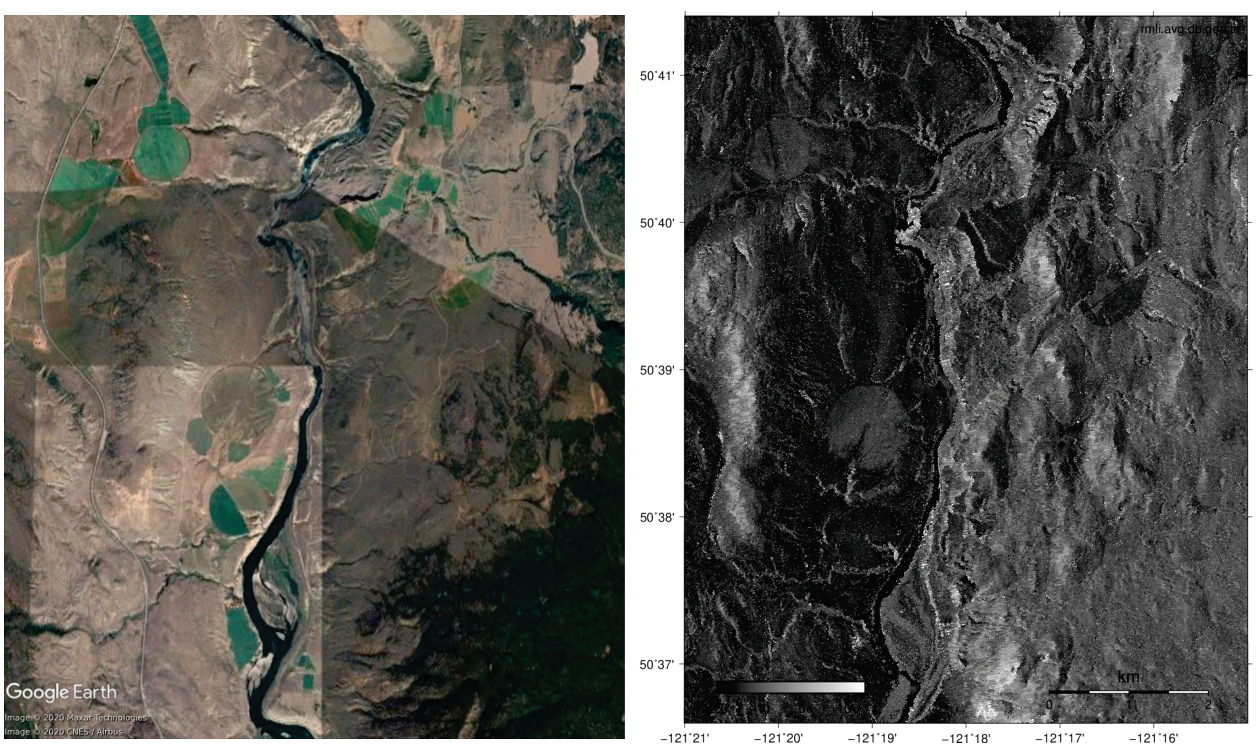

Figure 3: Optical (image credit: Google Earth) and Average Registered Multilook Intensity (RMLI) images

The SAR data used in this example has been acquired with the RCM 5M10 beam mode in HH polarization and with the Unity-Sigma lookup table (LUT). There are 8 image dates starting on March 4th, 2020 until April 13th, 2020. The data was processed with the automated DInSAR system. An example of the output file structure for the first three image dates is presented below. A list of filename acronyms is presented in Appendix B.

```
ThompsonRiver_Sigma_Asc_5M10.
├── bperp_file_insar
├── bperp_file_insar.pdf
├── insar
│   ├── 20200304_HH_20200308_HH
│   │   ├── 20200304_HH_20200308_HH.adf.cc.geo.kmz
│   │   ├── 20200304_HH_20200308_HH.adf.cc.geo.pdf
│   │   ├── 20200304_HH_20200308_HH.adf.cc.geo.tif
│   │   ├── 20200304_HH_20200308_HH.adf.wrp.geo.kmz
│   │   ├── 20200304_HH_20200308_HH.adf.wrp.geo.pdf
│   │   ├── 20200304_HH_20200308_HH.adf.wrp.geo.tif
│   │   ├── 20200304_HH_20200308_HH.disp.geo.kmz
│   │   ├── 20200304_HH_20200308_HH.disp.geo.pdf
│   │   ├── 20200304_HH_20200308_HH.disp.geo.tif
│   │   ├── 20200304_HH_20200308_HH.wrp.geo.kmz
│   │   ├── 20200304_HH_20200308_HH.wrp.geo.pdf
│   │   ├── 20200304_HH_20200308_HH.wrp.geo.tif
│   │   ├── 20200304_HH_lv_phi.geo.tif
│   │   └── 20200304_HH_lv_theta.geo.tif
│   ├── 20200304_HH_20200312_HH
│   │   ├── 20200304_HH_20200312_HH.adf.cc.geo.kmz
│   │   ├── 20200304_HH_20200312_HH.adf.cc.geo.pdf
│   │   ├── 20200304_HH_20200312_HH.adf.cc.geo.tif
│   │   ├── 20200304_HH_20200312_HH.adf.wrp.geo.kmz
│   │   ├── 20200304_HH_20200312_HH.adf.wrp.geo.pdf
│   │   ├── 20200304_HH_20200312_HH.adf.wrp.geo.tif
│   │   ├── 20200304_HH_20200312_HH.disp.geo.kmz
│   │   ├── 20200304_HH_20200312_HH.disp.geo.pdf
│   │   ├── 20200304_HH_20200312_HH.disp.geo.tif
│   │   ├── 20200304_HH_20200312_HH.wrp.geo.kmz
│   │   ├── 20200304_HH_20200312_HH.wrp.geo.pdf
│   │   ├── 20200304_HH_20200312_HH.wrp.geo.tif
│   │   ├── 20200304_HH_lv_phi.geo.tif
│   │   └── 20200304_HH_lv_theta.geo.tif
│   ├── 20200308_HH_20200312_HH
│   │   ├── 20200308_HH_20200312_HH.adf.cc.geo.kmz
│   │   ├── 20200308_HH_20200312_HH.adf.cc.geo.pdf
│   │   ├── 20200308_HH_20200312_HH.adf.cc.geo.tif
│   │   ├── 20200308_HH_20200312_HH.adf.wrp.geo.kmz
│   │   ├── 20200308_HH_20200312_HH.adf.wrp.geo.pdf
│   │   ├── 20200308_HH_20200312_HH.adf.wrp.geo.tif
│   │   ├── 20200308_HH_20200312_HH.disp.geo.kmz
│   │   ├── 20200308_HH_20200312_HH.disp.geo.pdf
```

```
│   │   ├── 20200308_HH_20200312_HH.disp.geo.tif
│   │   ├── 20200308_HH_20200312_HH.wrp.geo.kmz
│   │   ├── 20200308_HH_20200312_HH.wrp.geo.pdf
│   │   ├── 20200308_HH_20200312_HH.wrp.geo.tif
│   │   ├── 20200308_HH_lv_phi.geo.tif
│   │   └── 20200308_HH_lv_theta.geo.tif
├── rslc
│   ├── 20200304_HH_20200308_HH
│   │   └── geo
│   │       ├── 20200304_HH_dem.geo.kmz
│   │       ├── 20200304_HH_dem.geo.pdf
│   │       ├── 20200304_HH_dem.geo.tif
│   │       ├── 20200304_HH.rmli.geo.kmz
│   │       ├── 20200304_HH.rmli.geo.pdf
│   │       ├── 20200304_HH.rmli.geo.tif
│   │       ├── 20200308_HH.rmli.geo.kmz
│   │       ├── 20200308_HH.rmli.geo.pdf
│   │       └── 20200308_HH.rmli.geo.tif
│   ├── 20200304_HH_20200312_HH
│   │   └── geo
│   │       ├── 20200304_HH_dem.geo.kmz
│   │       ├── 20200304_HH_dem.geo.pdf
│   │       ├── 20200304_HH_dem.geo.tif
│   │       ├── 20200304_HH.rmli.geo.kmz
│   │       ├── 20200304_HH.rmli.geo.pdf
│   │       ├── 20200304_HH.rmli.geo.tif
│   │       ├── 20200312_HH.rmli.geo.kmz
│   │       ├── 20200312_HH.rmli.geo.pdf
│   │       └── 20200312_HH.rmli.geo.tif
│   ├── 20200308_HH_20200312_HH
│   │   └── geo
│   │       ├── 20200308_HH_dem.geo.kmz
│   │       ├── 20200308_HH_dem.geo.pdf
│   │       ├── 20200308_HH_dem.geo.tif
│   │       ├── 20200308_HH.rmli.geo.kmz
│   │       ├── 20200308_HH.rmli.geo.pdf
│   │       ├── 20200308_HH.rmli.geo.tif
│   │       ├── 20200312_HH.rmli.geo.kmz
│   │       ├── 20200312_HH.rmli.geo.pdf
│   │       └── 20200312_HH.rmli.geo.tif
├── ThompsonRiver_Asc_5M10_EODMS.xml
└── ts_insar
    ├── 20200304_HH_lv_phi.geo.tif
```

```
├── 20200304_HH_lv_theta.geo.tif
├── bperp_file_time_series
├── bperp_file_time_series.pdf
├── MSBAS_20200304T015031_LOS.kmz
├── MSBAS_20200304T015031_LOS.pdf
├── MSBAS_20200304T015031_LOS.tif
├── MSBAS_20200308T015031_LOS.kmz
├── MSBAS_20200308T015031_LOS.pdf
├── MSBAS_20200308T015031_LOS.tif
├── MSBAS_20200312T015031_LOS.kmz
├── MSBAS_20200312T015031_LOS.pdf
├── MSBAS_20200312T015031_LOS.tif
├── MSBAS_LINEAR_RATE_LOS.kmz
├── MSBAS_LINEAR_RATE_LOS.pdf
├── MSBAS_LINEAR_RATE_LOS.tif
├── MSBAS_LINEAR_RATE_R2_LOS.tif
├── MSBAS_LINEAR_RATE_STD_LOS.tif
├── MSBAS_LOG.txt
└── MSBAS_TSOUT.txt
```

For DInSAR processing, a DEM is required to remove the topographic phase. For automated DInSAR processing, three DEM choices are available: CDSM which covers regions in Canada south of latitude 60°N, CDEM which covers all of Canada and SRTM which covers the world between latitude 60°S and 60°N. For this analysis, an ASTER DEM with 30 meter ground resolution was used, as pictured in Figure 4.

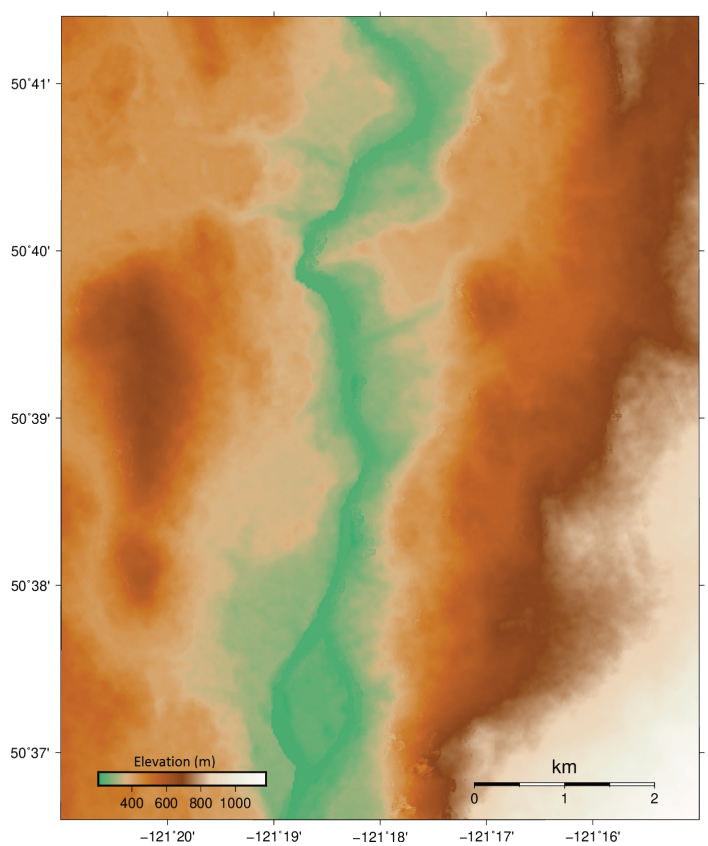

Figure 4: Digital elevation model

Forming interferograms between the image pairs creates the wrapped phase product. This product is then filtered to reduce phase noise using an adaptive spatial filter (Goldstein and Werner, 1998). The effects of this filtering are shown in Figure 5.

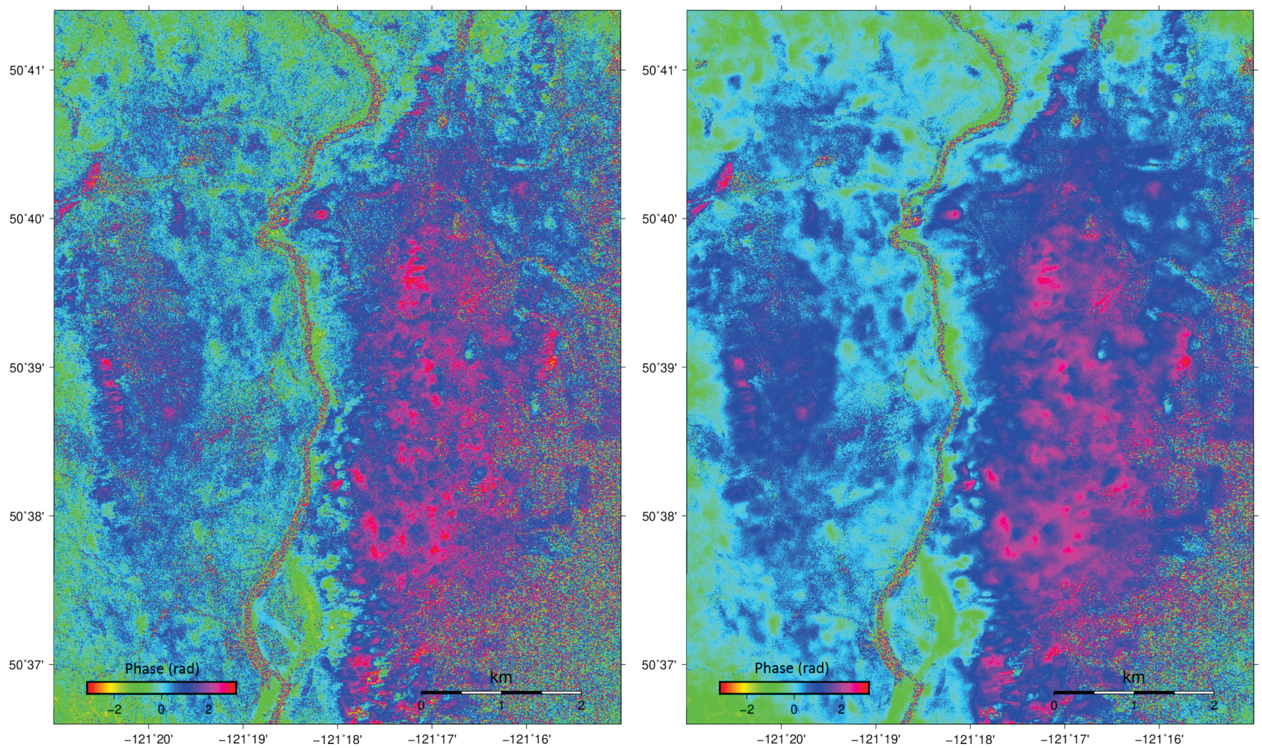

Figure 5: Wrapped interferometric phase before (left) and after (right) filtering.

Adaptive spatial filtering can be used to reduce noise and improved phase unwrapping results. However, temporal decorrelation still leads to a loss of coherence through time. The effect of this temporal decorrelation is shown in Figure 6.

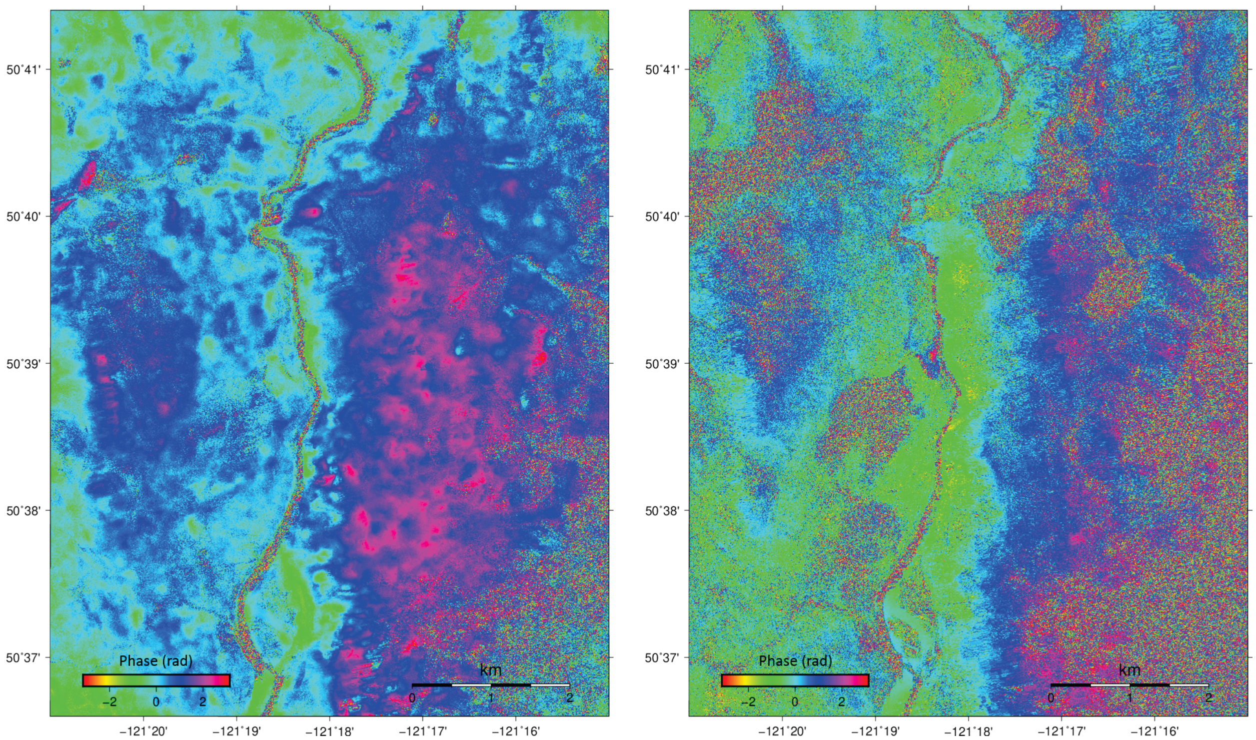

Figure 6: Filtered wrapped phase showing temporal decorrelation after 4 days (left) and 40 days (right).

After spatial filtering, the interferograms are unwrapped and the unwrapped phases are converted to a line-of-sight displacements, as shown in Figure 7.

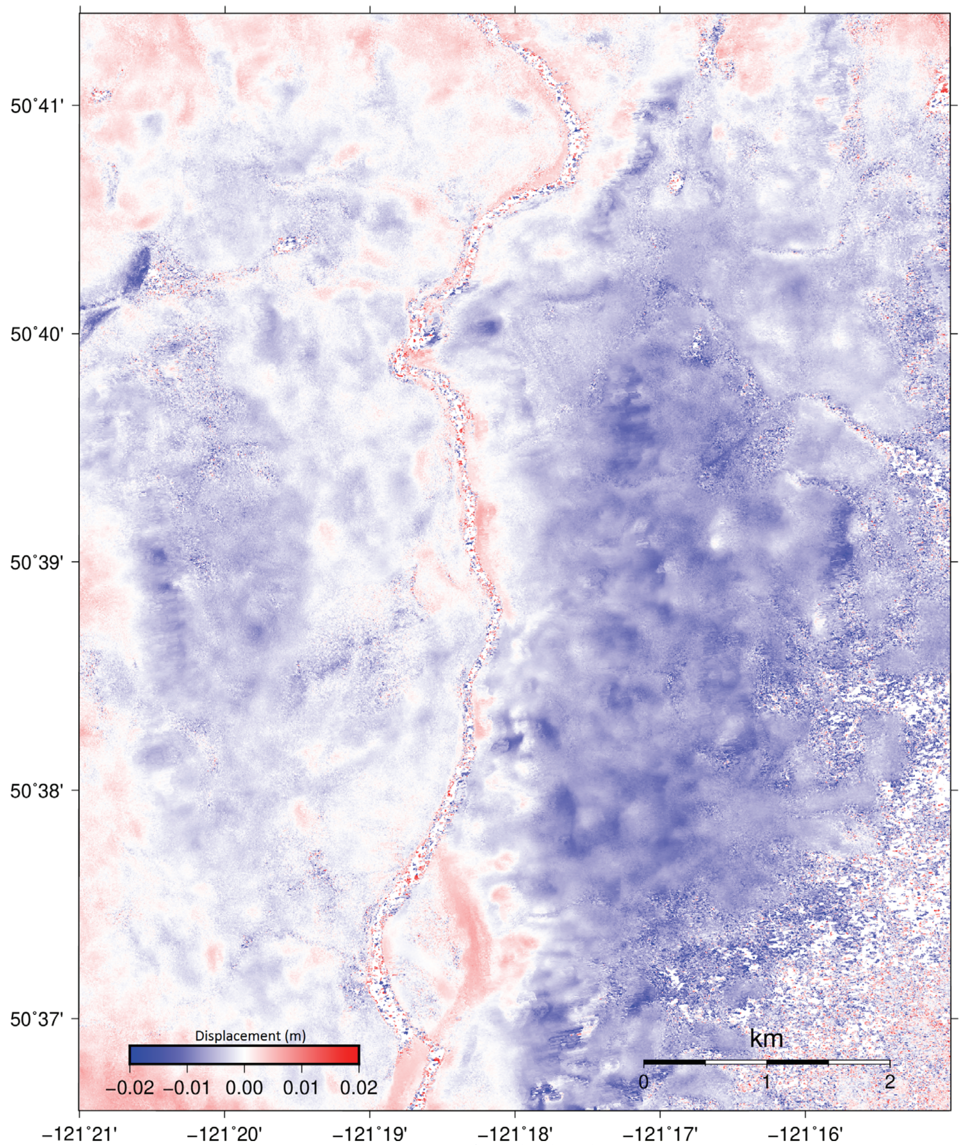

Figure 7: Line-of-sight displacement.

Residual noise from atmospheric and other phase noise sources can still be apparent in some displacement pairs. This noise is reduced when combined with other pairs in the Singular Value

Decomposition (SVD) performed in the MSBAS calculation, resulting in a cumulative line-of-sight ground deformation measurement, presented in Figure 8.

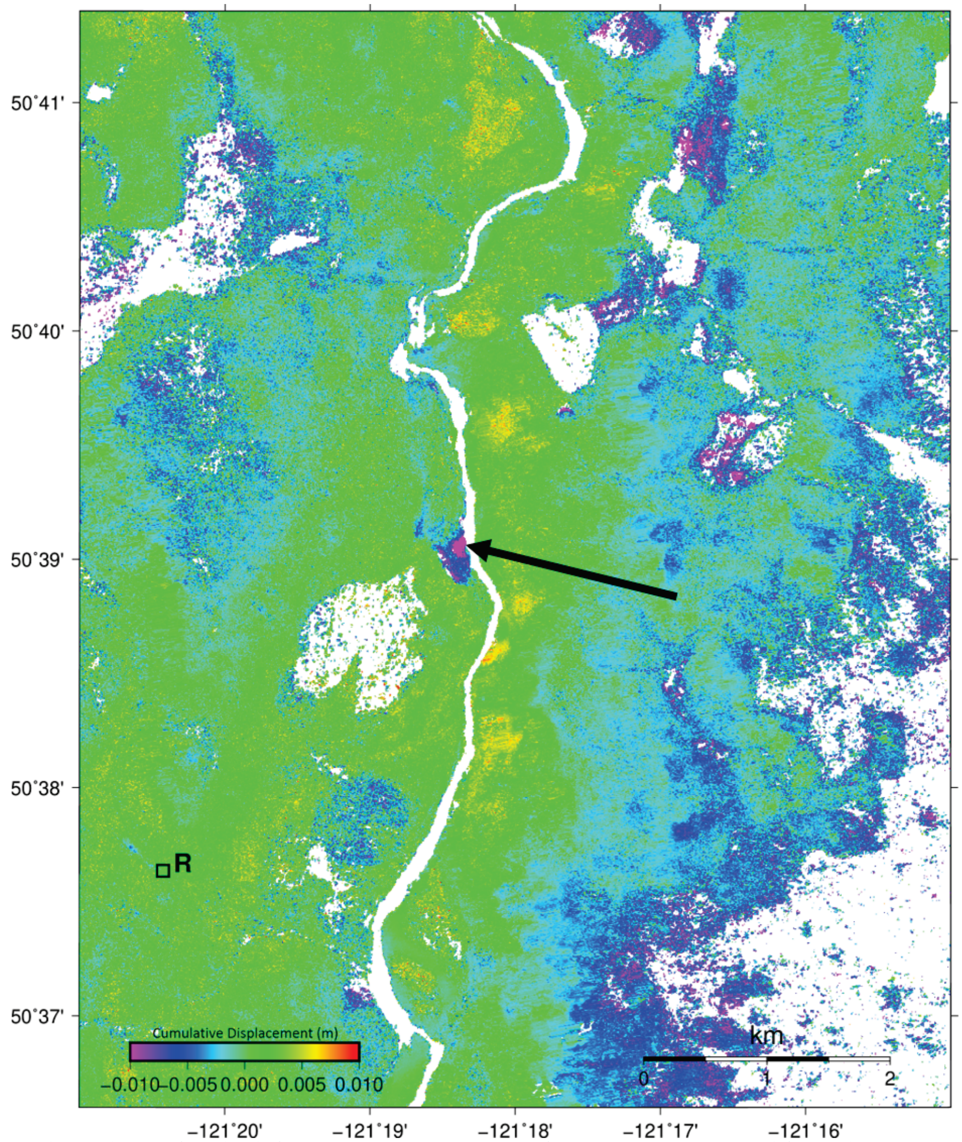

Figure 8: Cumulative line-of-sight deformation. Time series information is extracted from the region denoted by the arrow.

A stable reference region "R" is automatically selected and is used in the MSBAS algorithm to remove any residual phase offsets in the unwrapped interferograms.

Through the combination of multiple interferograms overlapping in time, transient noise sources are significantly reduced while the persistent signal is enhanced. Areas which have low coherence, possibly due to rapid changes in ground cover, are masked out of the cumulative results. For this example, several regions along the Thompson river indicate ground movement toward the river, possibly indicating landslides. Due to the line-of-sight nature of the measurement, movement on opposing sides of the river is in opposing directions. It is also possible to plot the time evolution of the ground movement at distinct points. Additional compatible software which provides this plotting functionality is also provided (Samsonov, 2019). An example of a time series plot using the GNUPLOT software package is presented in Figure 9.

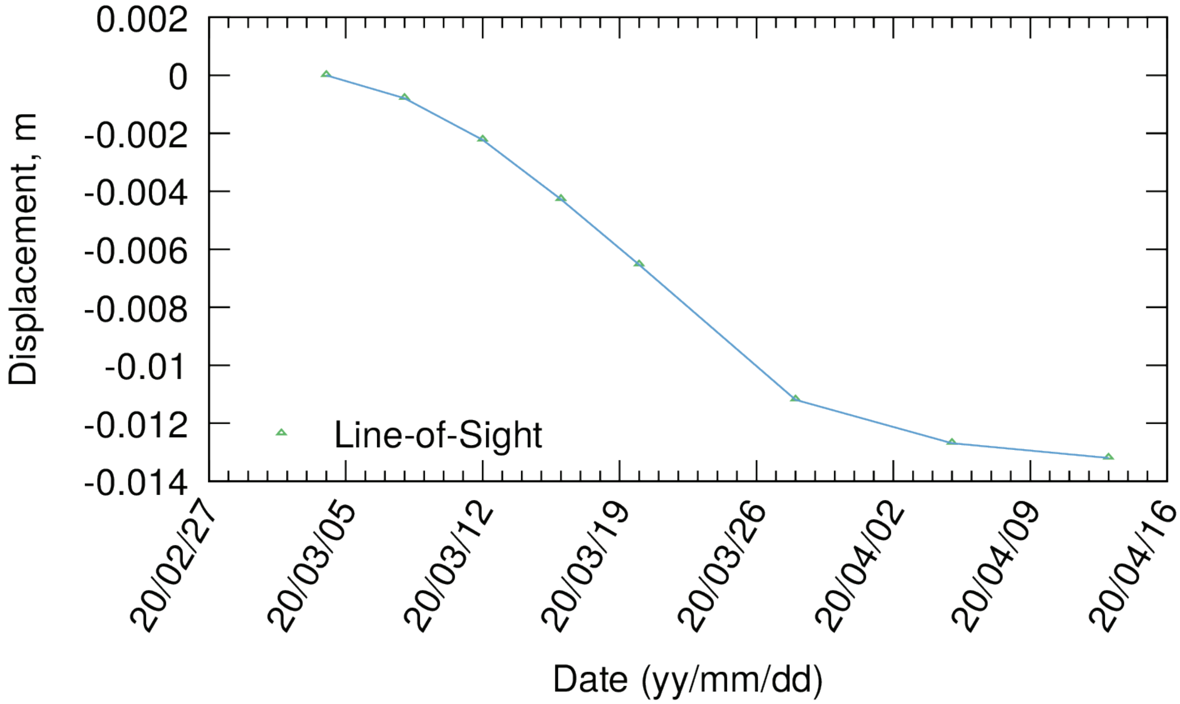

Figure 9: Line-of-sight time series displacement for the region shown in the cumulative deformation map.

5.2 SPO

Monitoring of glacial dynamics in Western Canada presents a unique challenge for remote sensing. In spring months, glacial flow can exhibit movement exceeding meters per day. For this type of rapid ground movement, traditional DInSAR monitoring is not possible as phase gradients are far too steep to unambiguously unwrap. In these cases, SPO methods can be effective. In this example, high resolution RADARSAT-2 data is used to monitor a wide region every 24 days. The region of interest is presented in both Google Earth optical imagery and an RMLI image from RADARSAT-2 in Figure 10.

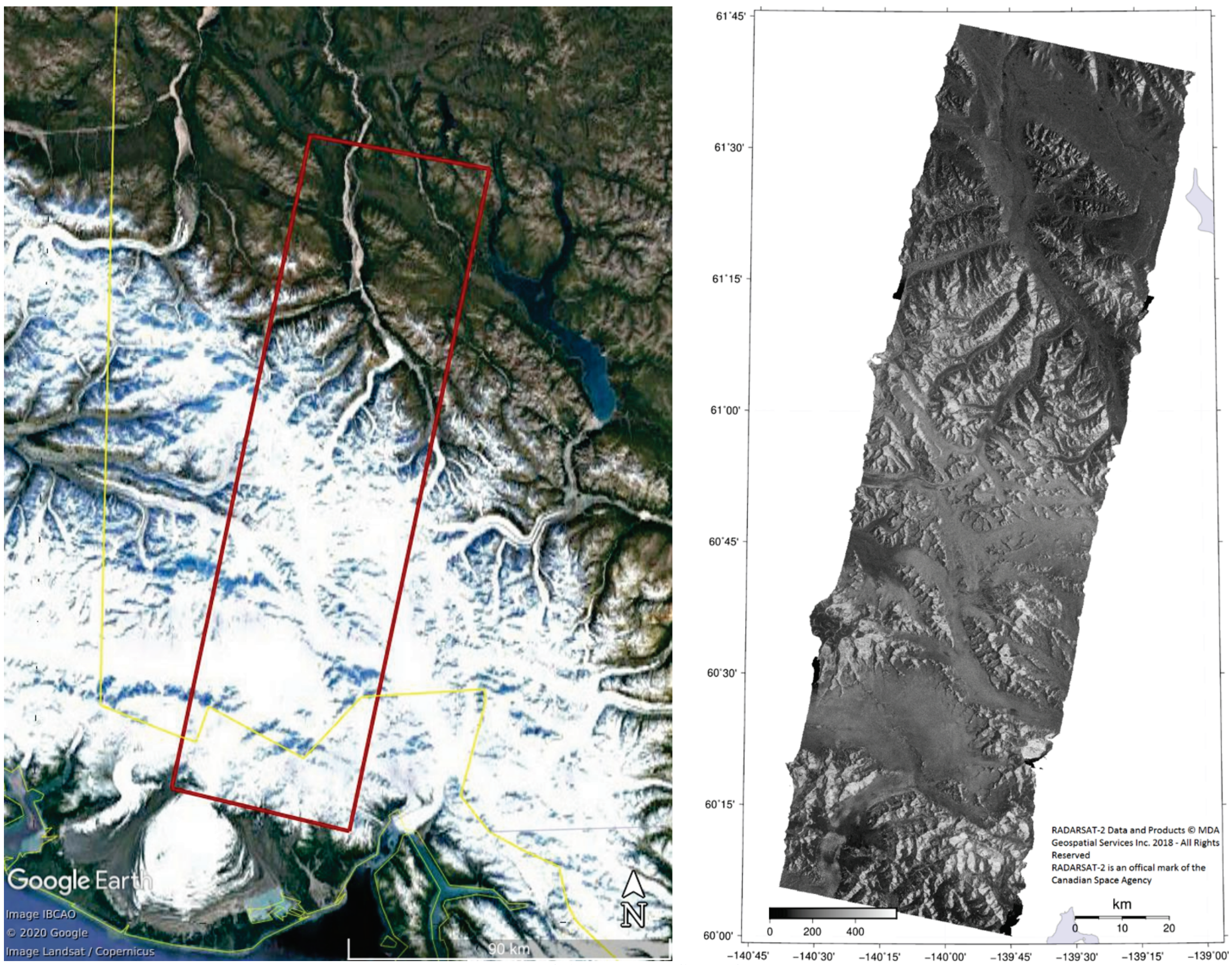

Figure 10: Optical (AOI in red) and RMLI images

The SAR data used in this example has been acquired with the RADARSAT-2 Ultrafine Wide beam mode in HH polarization and with the Sigma-nought lookup table. There are 4 image dates starting on January 6th, 2018 until March 19, 2018. The data was processed with the automated SPO system. An example of the output file structure for the first two image dates is presented below. A list of filename acronyms is presented in Appendix B.

```
Parks_Desc_U6W2
├── bperp_file_spo
├── bperp_file_spo.pdf
├── Parks_Desc_U6W2_EODMS.xml
├── rslc
│   └── 20180106_HH_20180130_HH
│       ├── geo
│       │   ├── 20180106_HH_dem.geo.kmz
│       │   ├── 20180106_HH_dem.geo.pdf
│       │   ├── 20180106_HH_dem.geo.tif
│       │   ├── 20180106_HH.rmli.geo.kmz
│       │   ├── 20180106_HH.rmli.geo.pdf
│       │   ├── 20180106_HH.rmli.geo.tif
│       │   ├── 20180130_HH.rmli.geo.kmz
│       │   ├── 20180130_HH.rmli.geo.pdf
│       │   └── 20180130_HH.rmli.geo.tif
│       └── geo_spo
│           ├── 20180106_HH_dem.geo.kmz
│           ├── 20180106_HH_dem.geo.pdf
│           ├── 20180106_HH_dem.geo.tif
│           ├── 20180106_HH.rmli.geo.kmz
│           ├── 20180106_HH.rmli.geo.pdf
│           ├── 20180106_HH.rmli.geo.tif
│           ├── 20180130_HH.rmli.geo.kmz
│           ├── 20180130_HH.rmli.geo.pdf
│           └── 20180130_HH.rmli.geo.tif
├── spo
│   └── 20180106_HH_20180130_HH
│       ├── 20180106_HH_20180130_HH.spo_azimuth.filtered.geo.kmz
│       ├── 20180106_HH_20180130_HH.spo_azimuth.filtered.geo.pdf
│       ├── 20180106_HH_20180130_HH.spo_azimuth.filtered.geo.tif
│       ├── 20180106_HH_20180130_HH.spo_azimuth.geo.kmz
│       ├── 20180106_HH_20180130_HH.spo_azimuth.geo.pdf
│       ├── 20180106_HH_20180130_HH.spo_azimuth.geo.tif
│       ├── 20180106_HH_20180130_HH.spo_ew.filtered.geo.kmz
│       ├── 20180106_HH_20180130_HH.spo_ew.filtered.geo.pdf
│       ├── 20180106_HH_20180130_HH.spo_ew.filtered.geo.tif
│       ├── 20180106_HH_20180130_HH.spo_magnitude.filtered.geo.kmz
│       ├── 20180106_HH_20180130_HH.spo_magnitude.filtered.geo.pdf
│       ├── 20180106_HH_20180130_HH.spo_magnitude.filtered.geo.tif
│       ├── 20180106_HH_20180130_HH.spo_ns.filtered.geo.kmz
│       ├── 20180106_HH_20180130_HH.spo_ns.filtered.geo.pdf
│       ├── 20180106_HH_20180130_HH.spo_ns.filtered.geo.tif
│       ├── 20180106_HH_20180130_HH.spo_range.filtered.geo.kmz
│       ├── 20180106_HH_20180130_HH.spo_range.filtered.geo.pdf
│       ├── 20180106_HH_20180130_HH.spo_range.filtered.geo.tif
│       │
```

```
│       ├── 20180106_HH_20180130_HH.spo_range.geo.kmz
│       ├── 20180106_HH_20180130_HH.spo_range.geo.pdf
│       ├── 20180106_HH_20180130_HH.spo_range.geo.tif
│       ├── 20180106_HH_20180130_HH.spo_snr.geo.kmz
│       ├── 20180106_HH_20180130_HH.spo_snr.geo.pdf
│       ├── 20180106_HH_20180130_HH.spo_snr.geo.tif
│       ├── 20180106_HH_20180130_HH.spo_ud.filtered.geo.kmz
│       ├── 20180106_HH_20180130_HH.spo_ud.filtered.geo.pdf
│       ├── 20180106_HH_20180130_HH.spo_ud.filtered.geo.tif
│       ├── 20180106_HH_dem_ddew.geo.tif
│       ├── 20180106_HH_dem_ddns.geo.tif
│       ├── 20180106_HH_lv_phi.geo.tif
│       └── 20180106_HH_lv_theta.geo.tif
├── ts_spo_3d
│   ├── 20180106_HH_dem_ddew.geo.tif
│   ├── 20180106_HH_dem_ddns.geo.tif
│   ├── 20180106_HH_lv_phi.geo.tif
│   ├── 20180106_HH_lv_theta.geo.tif
│   ├── bperp_file_time_series
│   ├── bperp_file_time_series.pdf
│   ├── MSBAS_20180106T154545_EW.tif
│   ├── MSBAS_20180106T154545_NS.tif
│   ├── MSBAS_20180106T154545_UD.tif
│   ├── MSBAS_20180130T154545_EW.kmz
│   ├── MSBAS_20180130T154545_EW.pdf
│   ├── MSBAS_20180130T154545_EW.tif
│   ├── MSBAS_20180130T154545_NS.kmz
│   ├── MSBAS_20180130T154545_NS.pdf
│   ├── MSBAS_20180130T154545_NS.tif
│   ├── MSBAS_20180130T154545_UD.kmz
│   ├── MSBAS_20180130T154545_UD.pdf
│   ├── MSBAS_20180130T154545_UD.tif
│   ├── MSBAS_LINEAR_RATE_EW.kmz
│   ├── MSBAS_LINEAR_RATE_EW.pdf
│   ├── MSBAS_LINEAR_RATE_EW.tif
│   ├── MSBAS_LINEAR_RATE_NS.kmz
│   ├── MSBAS_LINEAR_RATE_NS.pdf
│   ├── MSBAS_LINEAR_RATE_NS.tif
│   ├── MSBAS_LINEAR_RATE_R2_EW.tif
│   ├── MSBAS_LINEAR_RATE_R2_NS.tif
│   ├── MSBAS_LINEAR_RATE_R2_UD.tif
│   ├── MSBAS_LINEAR_RATE_STD_EW.tif
│   ├── MSBAS_LINEAR_RATE_STD_NS.tif
│   ├── MSBAS_LINEAR_RATE_STD_UD.tif
│   ├── MSBAS_LINEAR_RATE_UD.kmz
│   ├── MSBAS_LINEAR_RATE_UD.pdf
```

```
│   ├── MSBAS_LINEAR_RATE_UD.tif
│   ├── MSBAS_LOG.txt
│   └── MSBAS_TSOUT.txt
├── ts_spo_azimuth
│   ├── 20180106_HH_lv_phi.geo.tif
│   ├── 20180106_HH_lv_theta.geo.tif
│   ├── bperp_file_time_series
│   ├── bperp_file_time_series.pdf
│   ├── MSBAS_20180106T154545_LOS.tif
│   ├── MSBAS_20180130T154545_LOS.kmz
│   ├── MSBAS_20180130T154545_LOS.pdf
│   ├── MSBAS_20180130T154545_LOS.tif
│   ├── MSBAS_LINEAR_RATE_LOS.kmz
│   ├── MSBAS_LINEAR_RATE_LOS.pdf
│   ├── MSBAS_LINEAR_RATE_LOS.tif
│   ├── MSBAS_LINEAR_RATE_R2_LOS.tif
│   ├── MSBAS_LINEAR_RATE_STD_LOS.tif
│   ├── MSBAS_LOG.txt
│   └── MSBAS_TSOUT.txt
└── ts_spo_range
    ├── 20180106_HH_lv_phi.geo.tif
    ├── 20180106_HH_lv_theta.geo.tif
    ├── bperp_file_time_series
    ├── bperp_file_time_series.pdf
    ├── MSBAS_20180106T154545_LOS.tif
    ├── MSBAS_20180130T154545_LOS.kmz
    ├── MSBAS_20180130T154545_LOS.pdf
    ├── MSBAS_20180130T154545_LOS.tif
    ├── MSBAS_LINEAR_RATE_LOS.kmz
    ├── MSBAS_LINEAR_RATE_LOS.pdf
    ├── MSBAS_LINEAR_RATE_LOS.tif
    ├── MSBAS_LINEAR_RATE_R2_LOS.tif
    ├── MSBAS_LINEAR_RATE_STD_LOS.tif
    ├── MSBAS_LOG.txt
    └── MSBAS_TSOUT.txt
```

For this analysis, an ASTER DEM with 30 meter ground resolution was employed, shown in Figure 11.

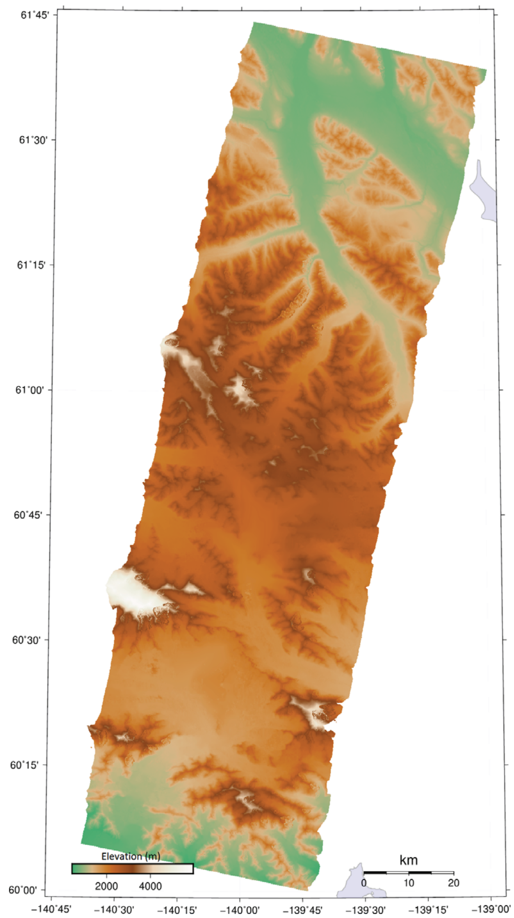

Figure 11: Digital elevation model

In SPO processing, movement is measured in the range and azimuth directions by cross-correlating pixels within a window between two image dates and calculating the offsets. Unlike the coherence measurement made in DInSAR processing, the quality of the SPO measurement can be quantified with the signal-to-noise (SNR) of the offsets. Regions with low SNR are not considered reliable measurements and are masked out. The range and azimuth offsets for a single date pair, along with the associated SNR are presented in Figure 12.

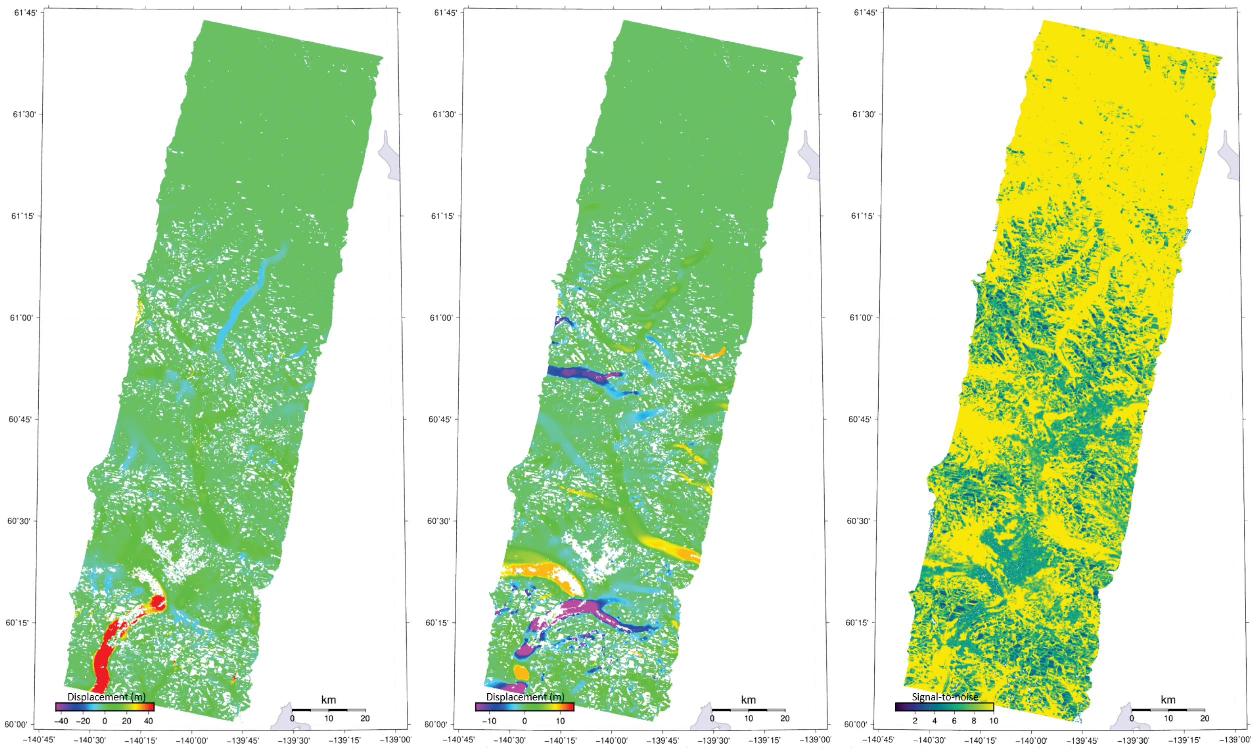

Figure 12: Azimuth, range, and SNR. Regions with low SNR (dark purple) are masked out.

From these maps, the large scale and rapid pace of glacial flows are apparent. Movement of more than 10 meters in a 24 day period is observed and could not be measured with traditional DInSAR techniques.

As mentioned earlier, the glacial flow is expected to follow the local topographic gradients. By adding this constraint to the azimuth and range measurements, three dimensional movements can be derived for this same 24 day period. This three dimensional movement is presented in Figure 13.

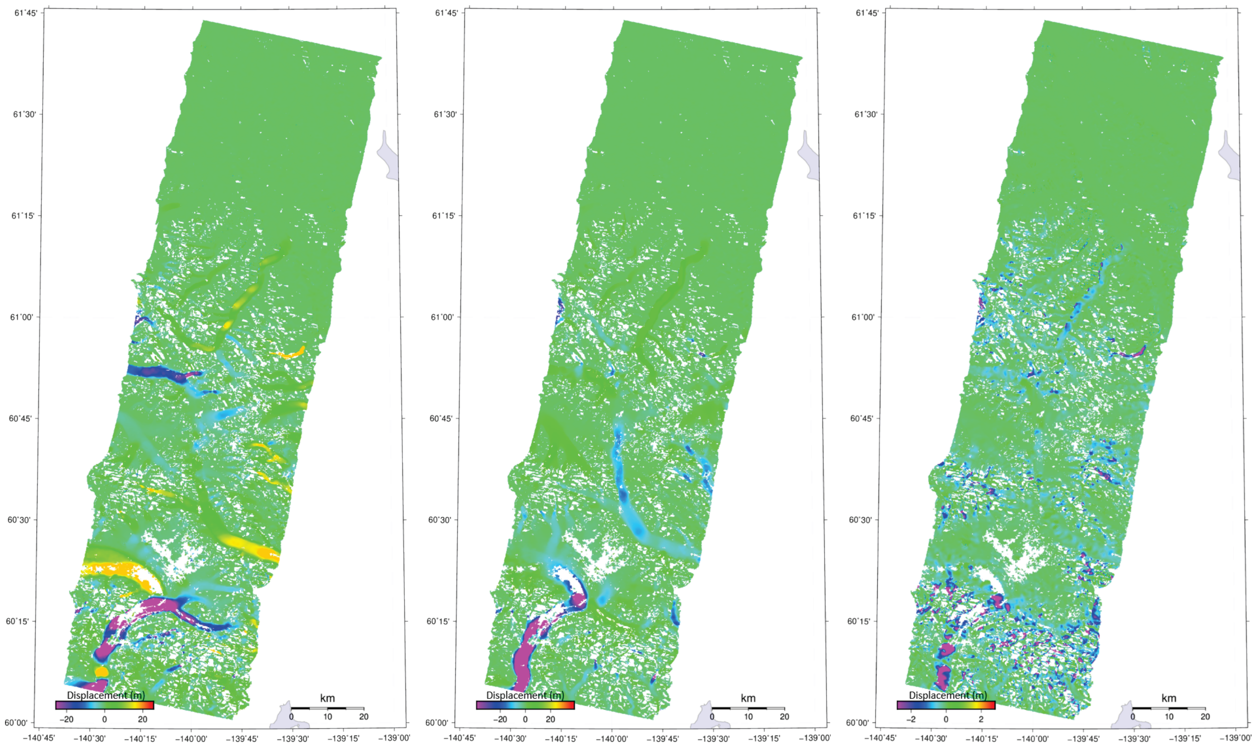

Figure 13: East/west, north/south, and up/down displacements.

For these glacial flow measurements, the majority of the movement is in the east/west and north/south directions with smaller displacements in the downward direction. To better visualize this, a magnitude displacement map can be created, as shown in Figure 14. In this map, the combined magnitude of all three displacements is mapped to a colour scale while the direction of surface movement is mapped to arrow vectors.

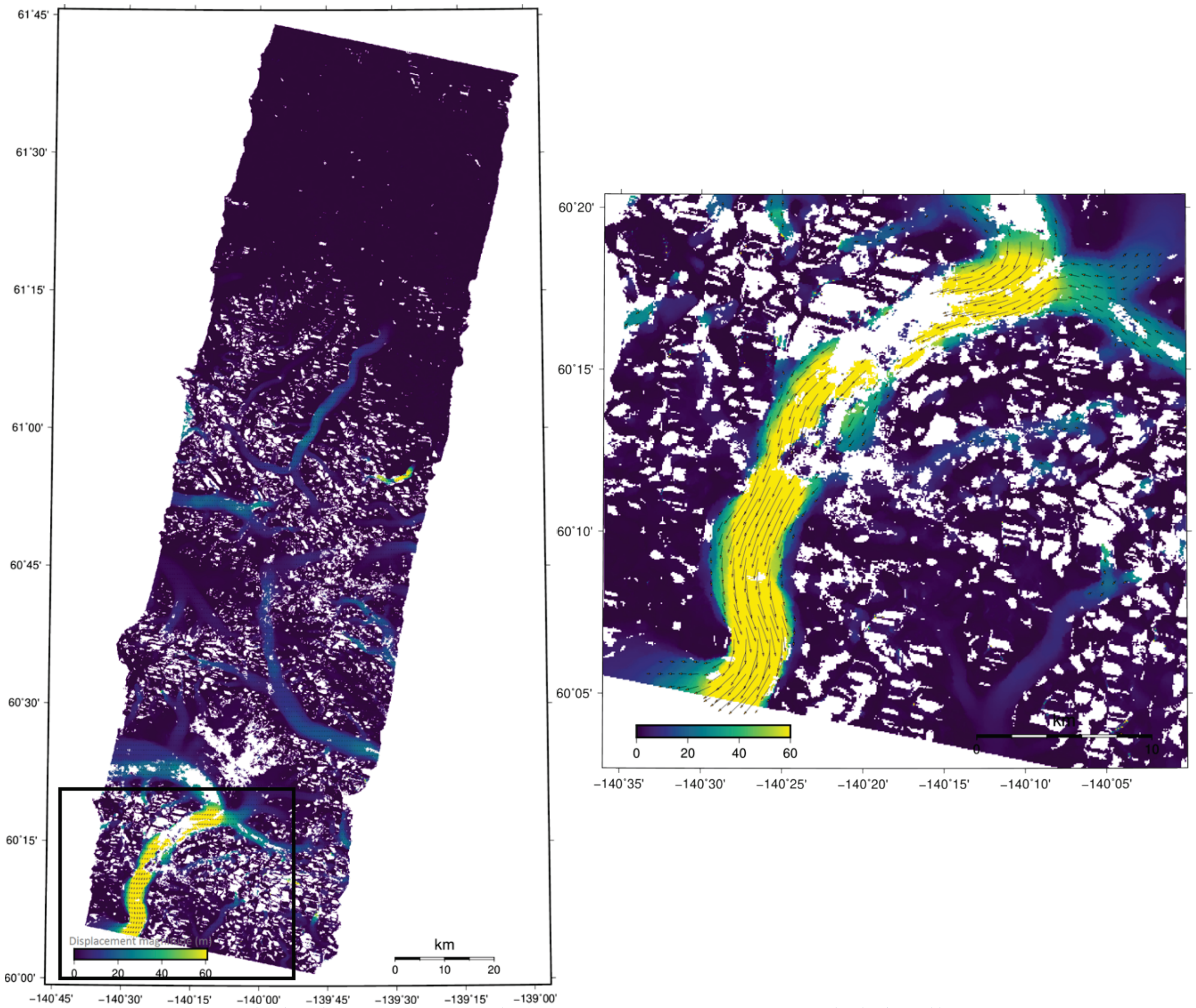

Figure 14: Magnitude displacement map with arrow vectors. Inset map is included to illustrate arrow vectors.

As with the DInSAR analysis technique, the discrete measurement across overlapping time periods can be combined to derive a cumulative measurement and time series. By combining measurements made over a 72 day period, cumulative displacements can be derived and are presented in Figure 15.

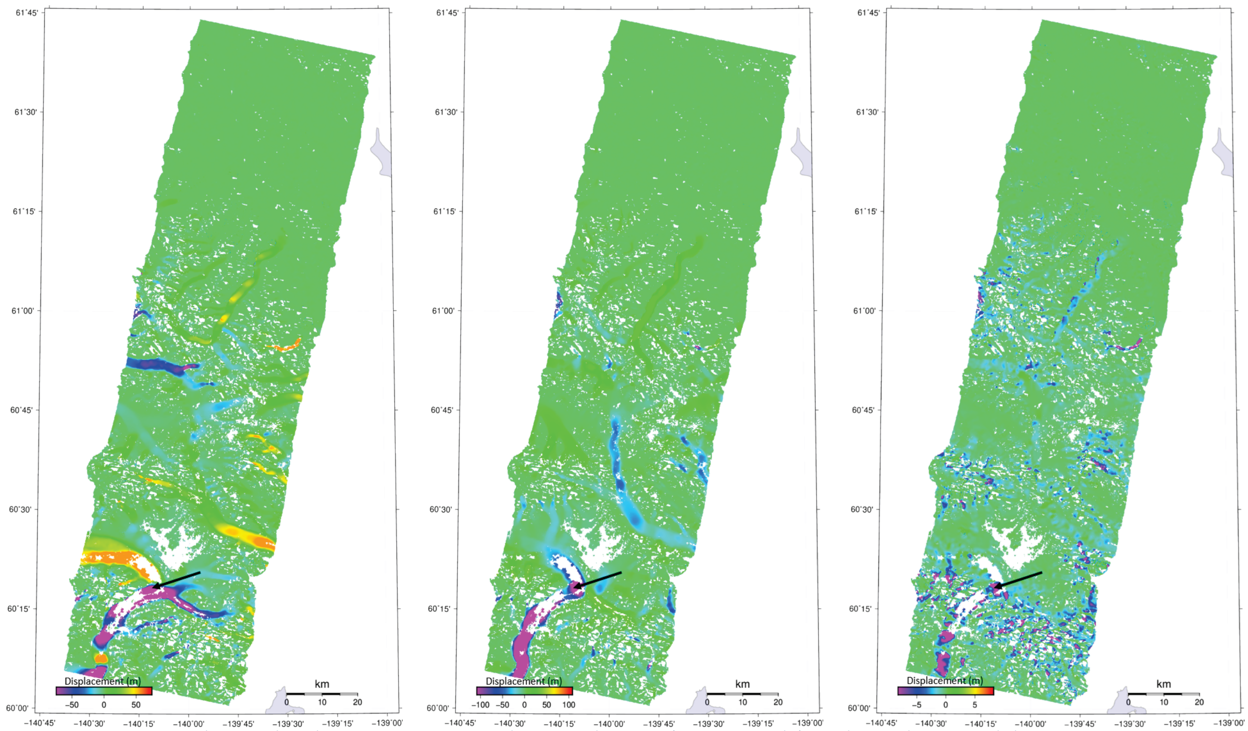

Figure 15: Cumulative displacement over 72 days in the east/west, north/south, and vertical directions. Time series information is extracted from the region denoted by the arrow.

The evolution of the displacement can also be expressed as a time series plot for an individual point using a variety of third party software, for example GNUPLOT, as shown in Figure 16.

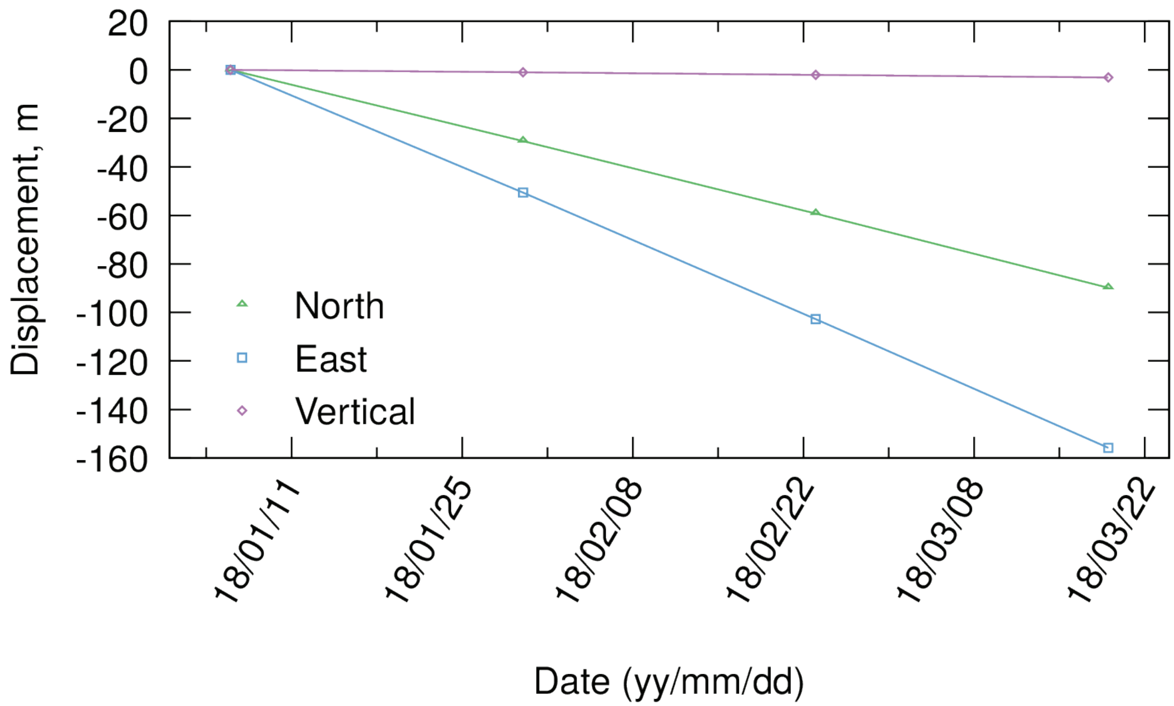

Figure 16: Time series of 3D displacement for the region shown in the cumulative deformation maps.

6. Conclusion

This document is intended to provide an introduction and user guide to users of the automated DInSAR VAP system. A brief background and summary of the DInSAR and SPO processing techniques has been provided so that users can familiarize themselves with the underlying principles. Spatial coherence and signal-to-noise were introduced as indicators of measurement quality for DInSAR and SPO techniques respectively.

A variety of potential applications where DInSAR and SPO techniques may be appropriate were introduced. DInSAR was shown to be most applicable in regions where the expected displacements change slowly (centimeters) with respect to the pixel size and temporal repeat interval. The use of SPO processing was shown to be useful in regions where the displacements are expected to be larger (meters) between repeat imaging.

A processing manual was introduced which described the characteristics of SAR data. This included descriptions of polarization, resolution, and imaging geometry. The available SAR modes for both RADARSAT-2 and RCM were presented in table form. Methods for ordering SAR data through the OHS as well as VAP data through EODMS were summarized. A full list of available DInSAR and SPO output products was also provided.

Two case studies were investigated showing potential uses for DInSAR and SPO. Using DInSAR and RCM data, gradual landslide activity in the Thompson River Valley was monitored and the time series evolution of the movement was derived. With the use of RADARSAT-2 data, rapid glacial flow was measured using SPO. The time series evolution in the east/west, north/south, and up/down directions was derived assuming a surface parallel flow constraint.

6.1 Future work

The automated DInSAR system will continue to be refined and optimized as its usage evolves. Updates will periodically be made to both the scripting software as well as the dependencies, including the GAMMA remote sensing software suite. Future support for persistent scatterer (PS) analysis will also be investigated.

6.2 Feedback address

For inquiries regarding the system software please contact:

Dr. Sergey V. SAMSONOV, Senior Research Scientist
Canada Centre for Mapping and Earth Observation, Natural Resources Canada
560 Rochester Street, Ottawa, ON K1S 5K2 Canada
Tel: 1-613-759-1186, Fax: 1-613-759-6344
Email: sergey.samsonov@canada.ca

Dr. Jonathan Dudley, Physical Scientist
Canada Centre for Remote Sensing, Natural Resources Canada
560 Rochester Street, Ottawa, ON K1S 5K2 Canada
Tel: 1-613-759-1891
Email: jonathan.dudley@canada.ca

6.3 Acknowledgements

We acknowledge the CSA for providing funding under the RCM Data Utilization and Applications Program (DUAP) as well as for providing access to RADARSAT-2 and RCM data. We thank and acknowledge Robert Landry and his team for developing the EODMS-VAP interface as an integral component of this project. We also thank and acknowledge Naomi Short, Bradley Lehrbass, Andrew Rotheram, and Nicolas Svacina for providing valuable feedback in reviewing this document. Images were plotted with GMT and GNUPLOT.

7. References

Bamler, R., and P. Hartl, 1998, Synthetic aperture radar interferometry Synthetic aperture radar interferometry: Inverse Problems, v. 14, no. 4, p. 55, doi:10.1088/0266-5611/14/4/001.

Bechor, N. B. D., and H. A. Zebker, 2006, Measuring two-dimensional movements using a single InSAR pair: Geophysical Research Letters, v. 33, no. 16, doi:10.1029/2006GL026883.

Berardino, R. P., G. Fornaro, R. Lanari, and E. Sansosti, 2002, new algorithm for surface deformation monitoring based on small baseline differential interferograms: IEEE Transactions on Geoscience and Remote Sensing, v. 40, no. 11, p. 23375–2383.

Jehle, M., Frey, O., Small, D. and Meier, E. 2010, Measurement of Ionospheric TEC in: IEEE Transactions on Geoscience and Remote Sensing, v. 48, no. 6, p. 2460–2468.

Ferretti, A., A. Monti-guarnieri, C. Prati, and F. Rocca, 2007, InSAR Principles: Guidelines for SAR Interferometry Processing and Interpretation (TM-19, February 2007): 71 p.

Ferretti, A., C. Prati, and F. Rocca, 2001, Permanent scatterers in SAR interferometry: IEEE Transactions on Geoscience and Remote Sensing, v. 39, no. 1, p. 8–20, doi:10.1109/36.898661.

Fialko, Y., M. Simons, and D. Agnew, 2001, The complete (3-D) surface displacement field in the epicentral area of the 1999 Mw 7.1 Hector Mine earthquake, California, from space geodetic observations: Geophysical Research Letters, v. 28, no. 16, p. 3063–3066, doi:10.1029/2001GL013174.

Goldstein, R., and Werner, C. 1998, Radar interferogram filtering for geophysical applications. Geophysical Research Letters, Vol.25(No. 21): pp. 4035–4038.

Gray, A. L., N. Short, K. E. Mattar, and K. C. Jezek, 2001, Velocities and Flux of the Filchner Ice Shelf and its Tributaries Determined from Speckle Tracking Interferometry: Canadian Journal of Remote Sensing, v. 27, no. 3, p. 193–206, doi:10.1080/07038992.2001.10854936.

Hanssen, R. F., 2002, RADAR Interferomotry: Data Interpretation and Error Analysis.

Hooper, A. J., 2008, A combined multi-temporal InSAR method incorporating persistent scatterer and small baseline approaches: Geophysical Research Letters, v. 35, no. 16, doi:10.1029/2008GL034654.

Hooper, A., D. Bekaert, K. Spaans, and M. Arikan, 2012, Recent advances in SAR interferometry time series analysis for measuring crustal deformation: Tectonophysics, v. 514–517, p. 1–13, doi:10.1016/j.tecto.2011.10.013.

Hooper, A., H. Zebker, P. Segall, and B. Kampes, 2004, A new method for measuring deformation on volcanoes and other natural terrains using InSAR persistent scatterers: Geophysical Research Letters, v. 31, no. 23, p. 1–5, doi:10.1029/2004GL021737.

Houghton, J. T., 1989, Introduction to the physics and techniques of remote sensing: Physics of the Earth and Planetary Interiors, v. 54, no. 1–2, p. 194, doi:10.1016/0031-9201(89)90201-X.

Jiang, M., Z. W. Li, X. L. Ding, J. J. Zhu, and G. C. Feng, 2011, Modeling minimum and maximum detectable deformation gradients of interferometric SAR measurements: International Journal of Applied Earth Observation and Geoinformation, v. 13, no. 5, p. 766–777, doi:10.1016/j.jag.2011.05.007.

Jung, H.-S., W.-J. Lee, and L. Zhang, 2014, Theoretical accuracy of along-track displacement measurements from multiple-aperture interferometry (MAI): Sensors (Switzerland), v. 14, no. 9, p.17703–17724, doi:10.3390/s140917703.

Lanari, R., O. Mora, M. Manunta, J. J. Mallorqui, P. Berardino, and E. Sansosti, 2004, A small-baseline approach for investigating deformations on full-resolution differential SAR interferograms: IEEE Transactions on Geoscience and Remote Sensing, v. 42, no. 7, p. 1377–1386, doi:10.1109/TGRS.2004.828196.

Li, Z., E. J. Fielding, P. Cross, and J.-P. Muller, 2006, Interferometric synthetic aperture radar atmospheric correction: GPS topography-dependent turbulence model: Journal of Geophysical Research: Solid Earth, v. 111, no. 2, doi:10.1029/2005JB003711.

Li, Z., J.-P. Muller, P. Cross, and E. J. Fielding, 2005, Interferometric synthetic aperture radar (InSAR) atmospheric correction: GPS, Moderate Resolution Imaging Spectroradiometer (MODIS), and InSAR integration: Journal of Geophysical Research B: Solid Earth, v. 110, no. 3, p. 1–10, doi:10.1029/2004JB003446.

Lubin, D., and R. Massom, 2007, Remote sensing of earth's polar regions: Opportunities for computational science: p. 58–71, doi:10.1109/MCSE.2007.16.

Massonnet, D., and K. L. Feigl, 1998, Radar interferometry and its application to changes in the Earth's surface: Reviews of Geophysics, v. 36, no. 4, p. 441–500, doi:10.1029/97RG03139.

Michel, R., and J.-P. Avouac, 1999, Measuring near field coseismic displacement from SAR images: application to the Landers earthquake: p. 3017–3020.

Samsonov, S., and N. d'Oreye, 2012, Multidimensional time-series analysis of ground deformation from multiple InSAR data sets applied to Virunga Volcanic Province: Geophysical Journal International, v. 191, no. 3, p. 1095–1108, doi:10.1111/j.1365-246X.2012.05669.x.

Samsonov, S., M. van der Kooij, and K. Tiampo, 2011, A simultaneous inversion for deformation rates and topographic errors of DInSAR data utilizing linear least square inversion technique: Computers and Geosciences, v. 37, no. 8, p. 1083–1091, doi:10.1016/j.cageo.2011.01.007.

Samsonov, S. V., A. P. Trishchenko, K. Tiampo, P. J. González, Y. Zhang, and J. Fernández, 2014, Removal of systematic seasonal atmospheric signal from interferometric synthetic aperture radar ground deformation time series: Geophysical Research Letters, v. 41, no. 17, p. 6123–6130, doi:10.1002/2014GL061307.

Samsonov, S V, 2019, User manual, source code, and test set for MSBASv3 (Multidimensional Small Baseline Subset version 3) for one- and two-dimensional deformation analysis: Geomatics Canada, Open File 45, doi.org/10.4095/313749.

Short, N. H., and A. L. Gray, 2005, Glacier dynamics in the Canadian High Arctic from RADARSAT-1 speckle tracking: Canadian Journal of Remote Sensing, v. 31, no. 3, p. 225–239, doi:10.5589/m05-010.

Short, N. H., and A. L. Gray, 2004, Potential for RADARSAT-2 interferometry: Glacier monitoring using speckle tracking: Canadian Journal of Remote Sensing, v. 30, no. 3, p. 504–509, doi:10.5589/m03-071.

Singleton, A., Z. Li, T. Hoey, and J.-P. Muller, 2014, Evaluating sub-pixel offset techniques as an alternative to D-InSAR for monitoring episodic landslide movements in vegetated terrain: Remote Sensing of Environment, v. 147, p. 133–144, doi:10.1016/j.rse.2014.03.003.

Strozzi, T., A. Luckman, T. Murray, U. Wegmuller, and C. L. Werner, 2002, Glacier motion estimation using SAR offset-tracking procedures: IEEE Transactions on Geoscience and Remote Sensing, v. 40, no. 11, p. 2384–2391, doi:10.1109/TGRS.2002.805079.

Strozzi, T., U. Wegmüller, C. Werner, A. Wiesmann, and M. Santoro, 2007, Potential of a C-band SAR mission with 12-day repeat cycle to derive ice surface velocity with interferometry and offset tracking, in International Geoscience and Remote Sensing Symposium (IGARSS): p. 4229–4232, doi:10.1109/IGARSS.2007.4423784.

Touzi, R., A. Lopes, J. Bruniquel, and P. W. Vachon, 1999, Coherence estimation for SAR imagery: IEEE Transactions on Geoscience and Remote Sensing, v. 37, no. 1 PART 1, p. 135–149, doi:10.1109/36.739146.

Van Wychen, W., L. Copland, L. Gray, D. Burgess, B. Danielson, and M. Sharp, 2012, Spatial and temporal variation of ice motion and ice flux from Devon Ice Cap, Nunavut, Canada: Journal of Glaciology, v. 58, no. 210, p. 657–664, doi:10.3189/2012JoG11J164.

Yun, S.-H., H. Zebker, P. Segall, A. Hooper, and M. Poland, 2007, Interferogram formation in the presence of complex and large deformation: Geophysical Research Letters, v. 34, no. 12, doi:10.1029/2007GL029745.

Zebker, H. A., and J. Villasenor, 1992, Decorrelation in Inteferometric Radar Echoes: IEEE Transactions on Geoscience and Remote Sensing, v. 30, no. 5, p. 950–959.

Appendix A: EODMS DInSAR Tutorial

The online interface for the automate DInSAR VAP system is integrated into The Earth Observation Data Management System (EODMS). This site can be found at: https://www.eodms-sgdot.nrcan-rncan.gc.ca/index_en.jsp with the main landing page shown below:

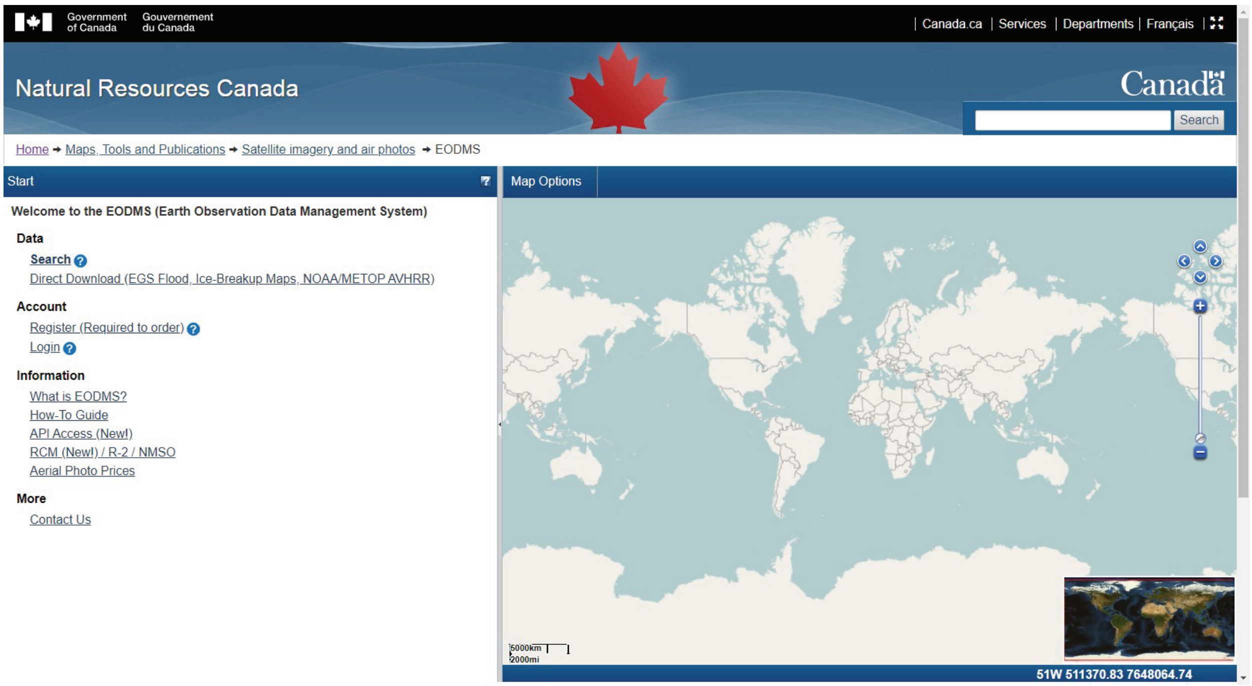

EODMS and VAP Access

Users will have to create accounts with EODMS and be approved for use of RADARSAT-2 and/or RCM SAR data products. Once an EODMS account has been made, the user can log into the system. Once logged in, various search and account options can be selected:

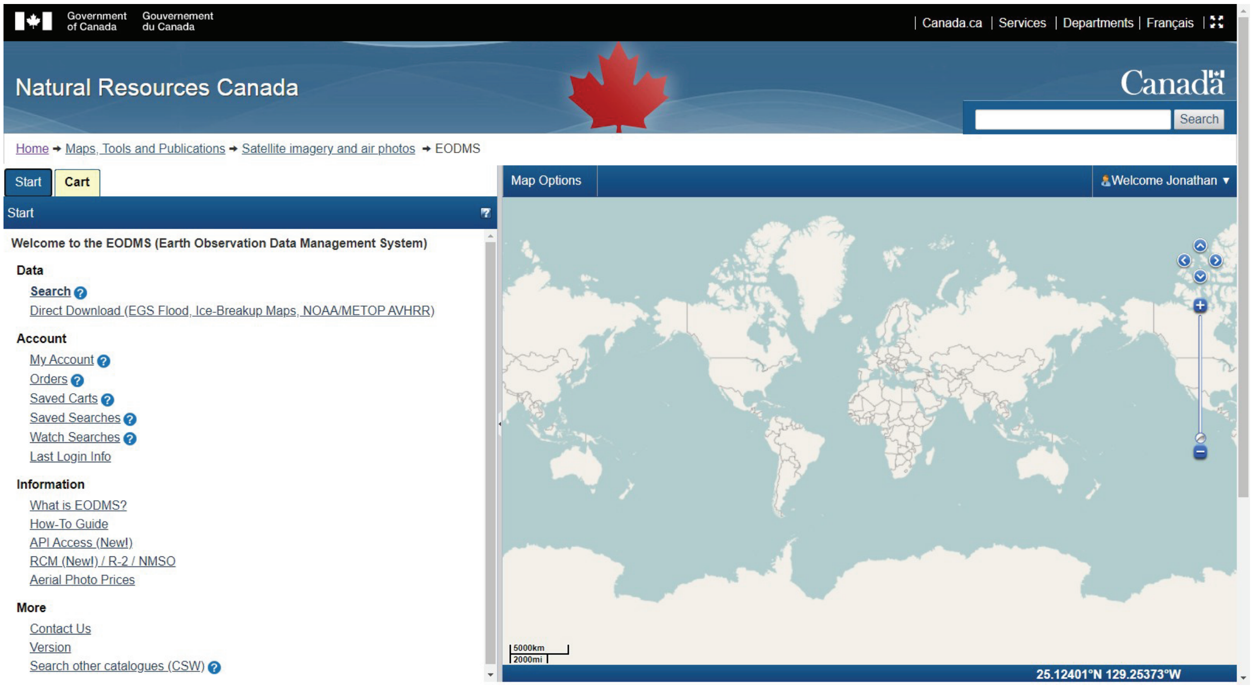

Sensor Selection

Prior to DInSAR processing, users must select their input data from the catalog. The first step in data selection is to select a sensor (RADARSAT-2 or RCM products). For this example, RCM data has been selected.

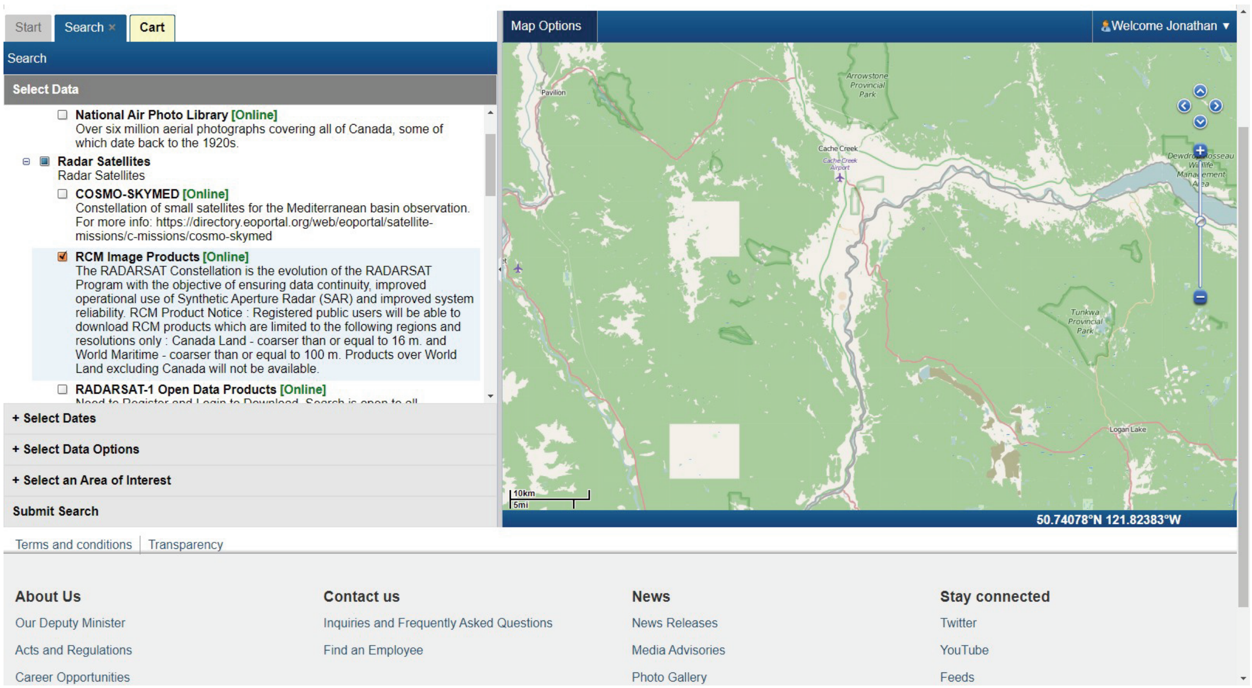

Date Selection

Next, the range of dates for the desired data can be selected. Only data within the date range will be included in the search.

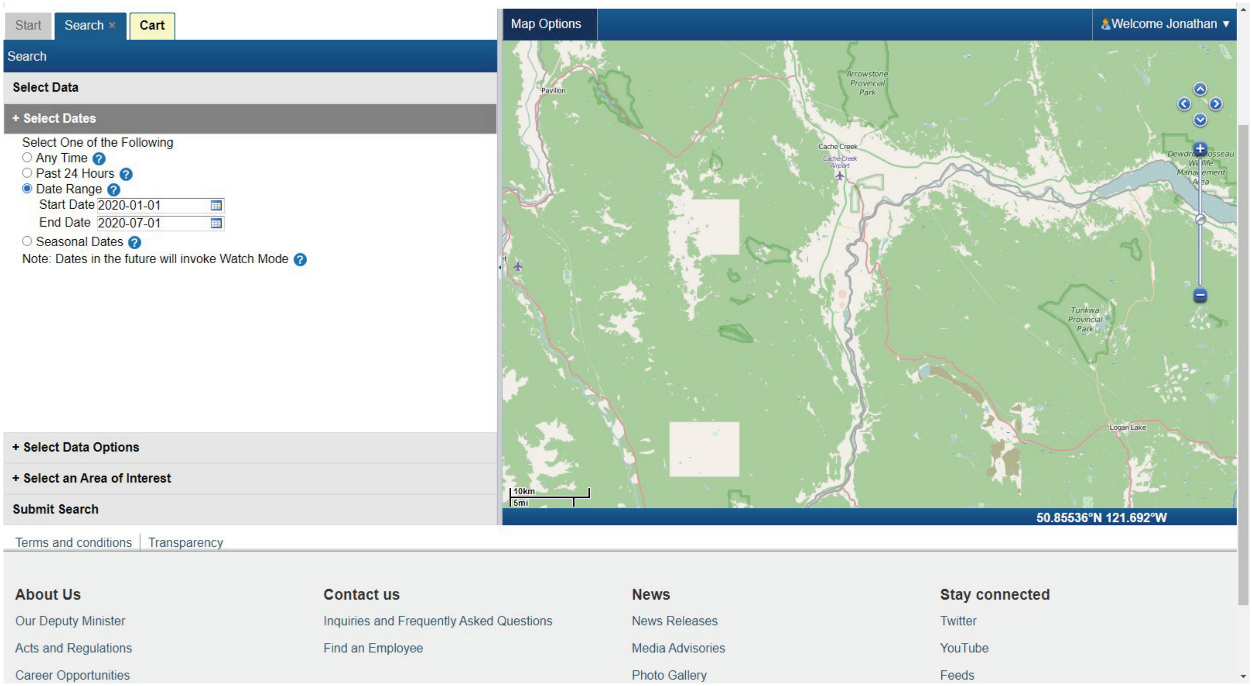

Beam Modes

The beam mode can be specified by its imaging geometry or by its mnemonic (if known). This will define the resolution and swath width of the data. A full list of RADARSAT-2 and RCM SLC beam modes can be found in Table 4 and Table 5. In general, it is recommended to select the beam mode with the finest resolution which still covers the area of interest.

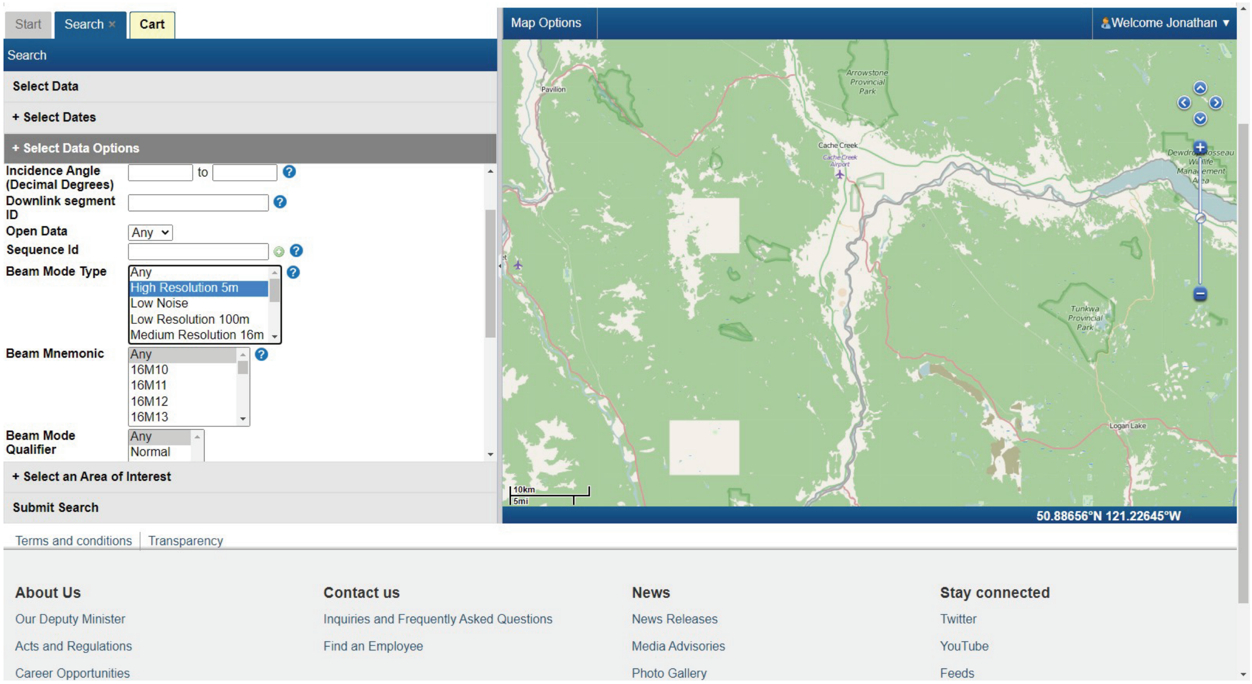

Polarization and Product Type

The polarization and product type are then defined. For DInSAR and SPO processing, single polarization (HH or VV) is recommended. The Product Type must be SLC (Single Look Complex).

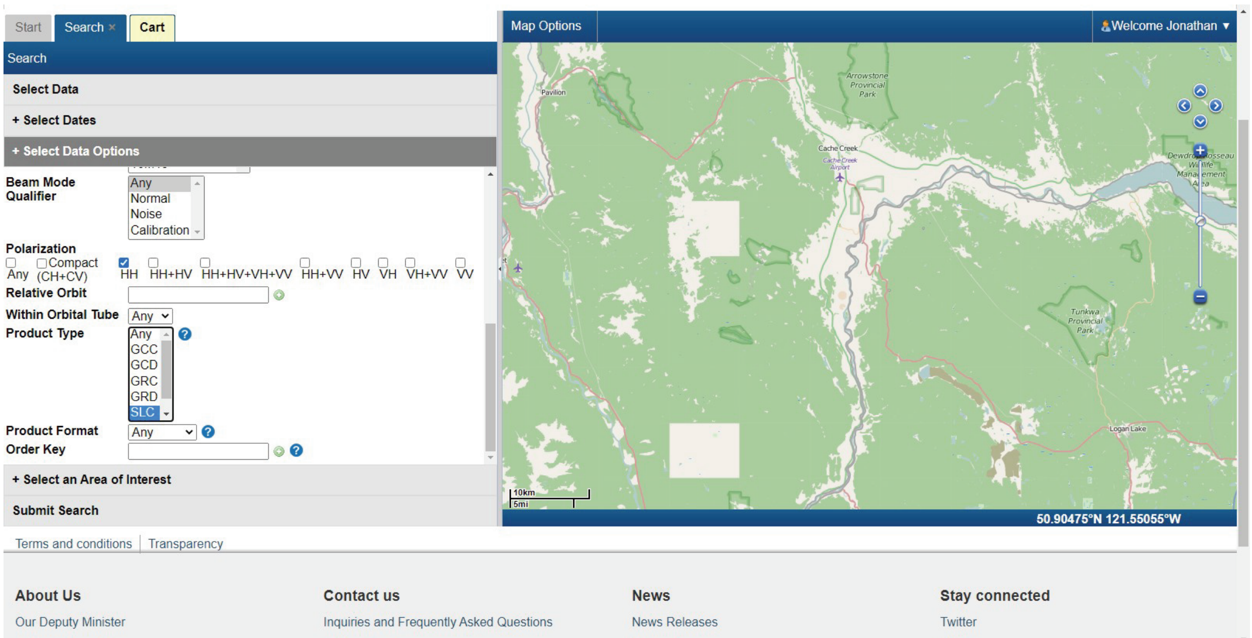

Area of Interest

Once the product specifications have been made, the area of interest (AOI) can be defined. This can be done through a variety of methods, as shown in the image. This area of interest will be used to locate the specified beam modes which intersect it. Note that this intersection does not guarantee total coverage. Once the search is complete the user can view the beam footprint overlap and select an appropriate beam mode.

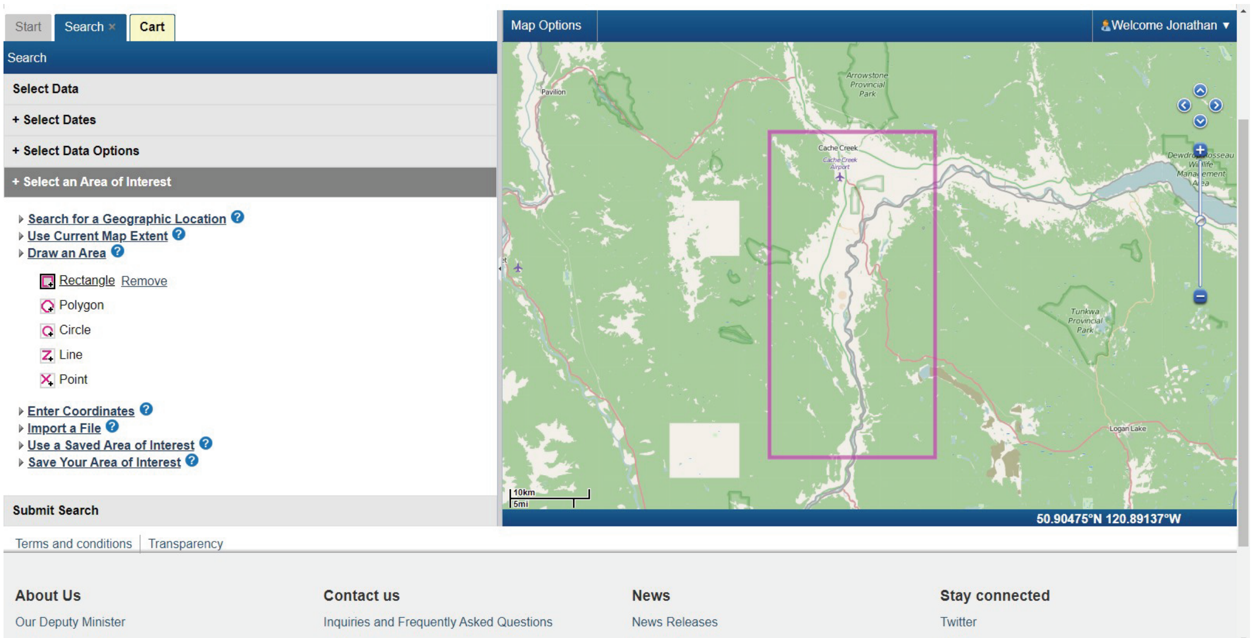

Image Search

Once the AOI has been defined, the image search can be initiated with the "Search" button. The EODMS system will indicate the search progress and the number of images which satisfy all of the search criteria.

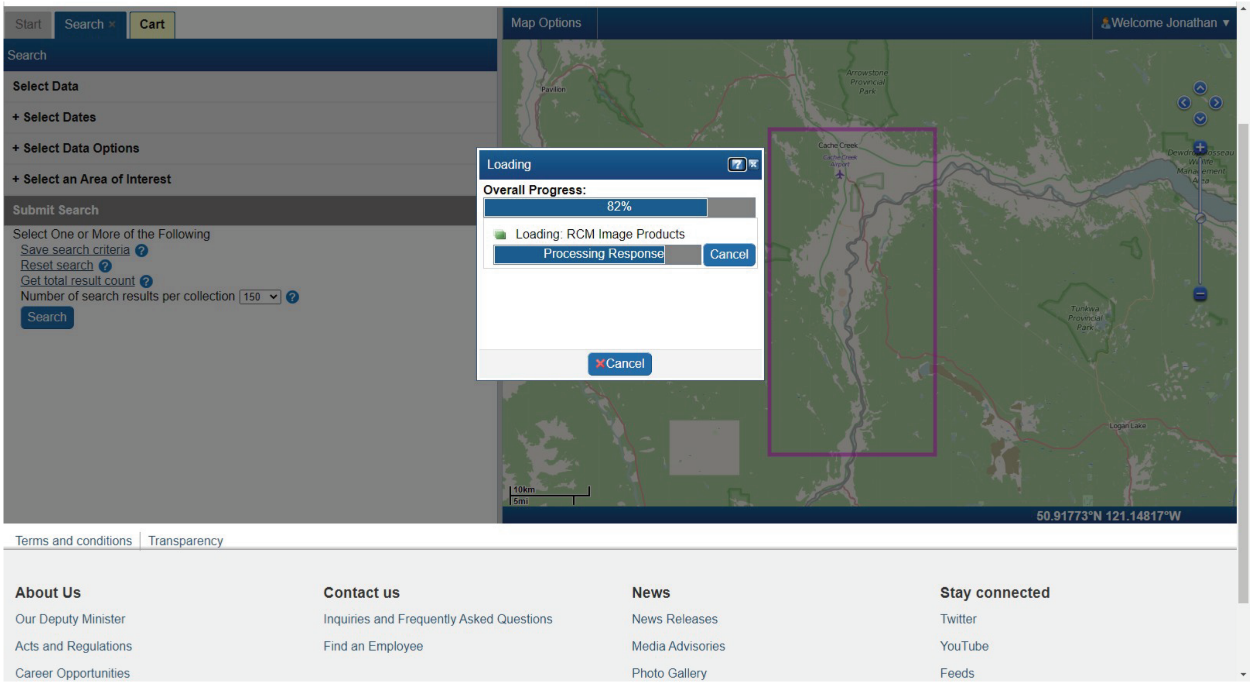

Search Results

Once the search has completed, the results of the search will be shown in both a table and a map format. The table will have information related to the sensor, dates, and beam mode characteristics. The map will show the footprints of the various beams and their intersection with the selected AOI. At this step the user can view the different beam options and footprints and then select the most appropriate mode and image dates.

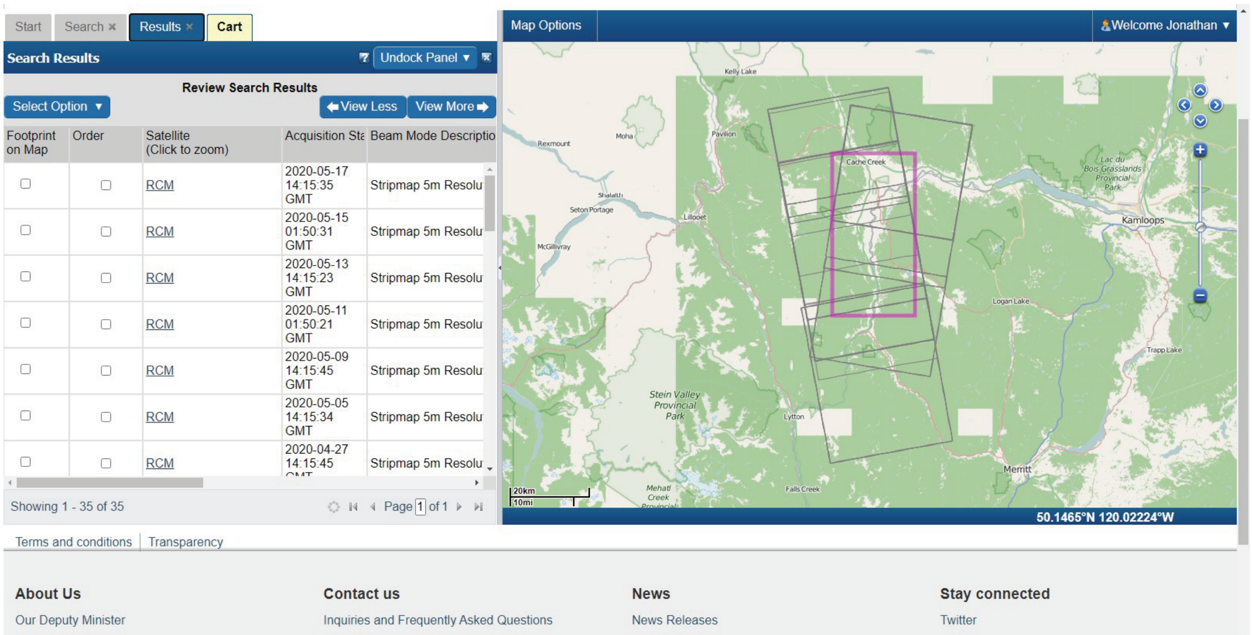

Search Selection

To select an image the “Order” checkbox must be selected for each image. When this checkbox is selected, an “Order Option” window will appear and the “Select Item” checkbox must be selected followed by the “Update Cart” button. For DInSAR processing, it is required that each selected image has the same footprint in the map window. Images which do not overlap exactly cannot be processed. All images must also be from the same beam mode and pass direction (Ascending or Descending) with matching LUTs.

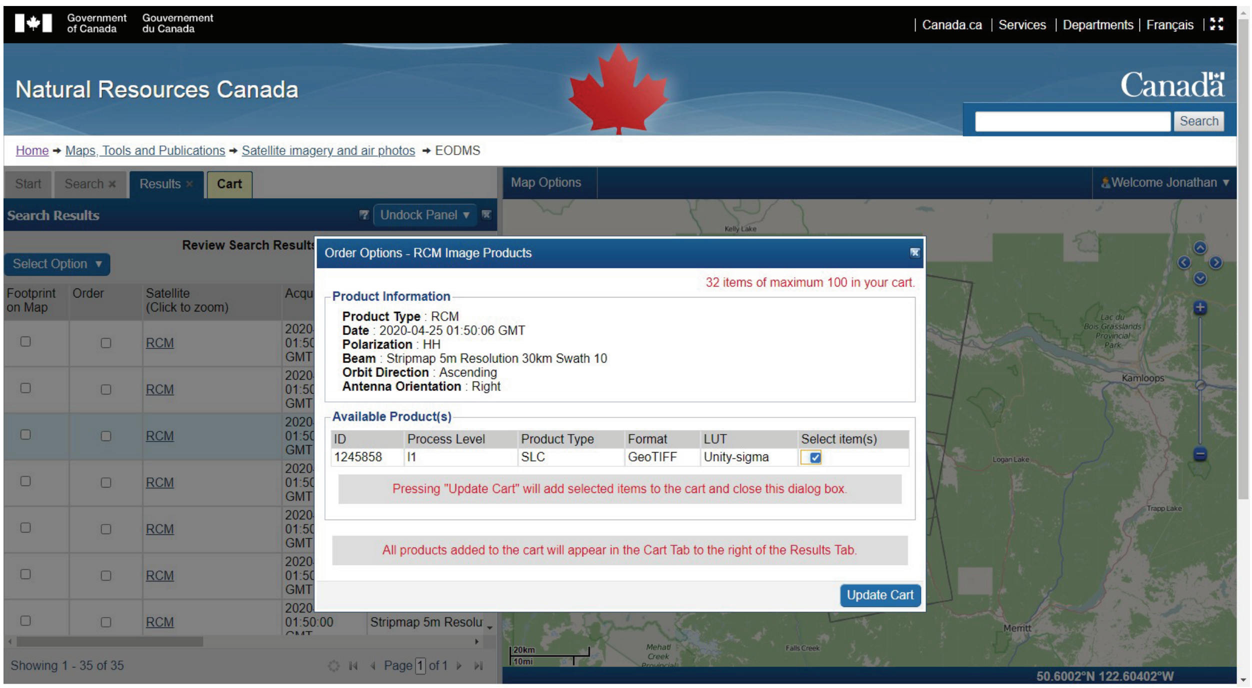

Cart Selection:

Once all of the images have been selected and added to the Cart, the “Cart” menu tab can be selected. This tab allows the user to select images for either direct download (through FTP) or for additional VAP processing. To add images to an DInSAR processing request, the “Product Selection” checkbox must be selected for all images to be processed. As before, the images footprints must all overlap, all images must be from the same beam mode and the same pass direction.

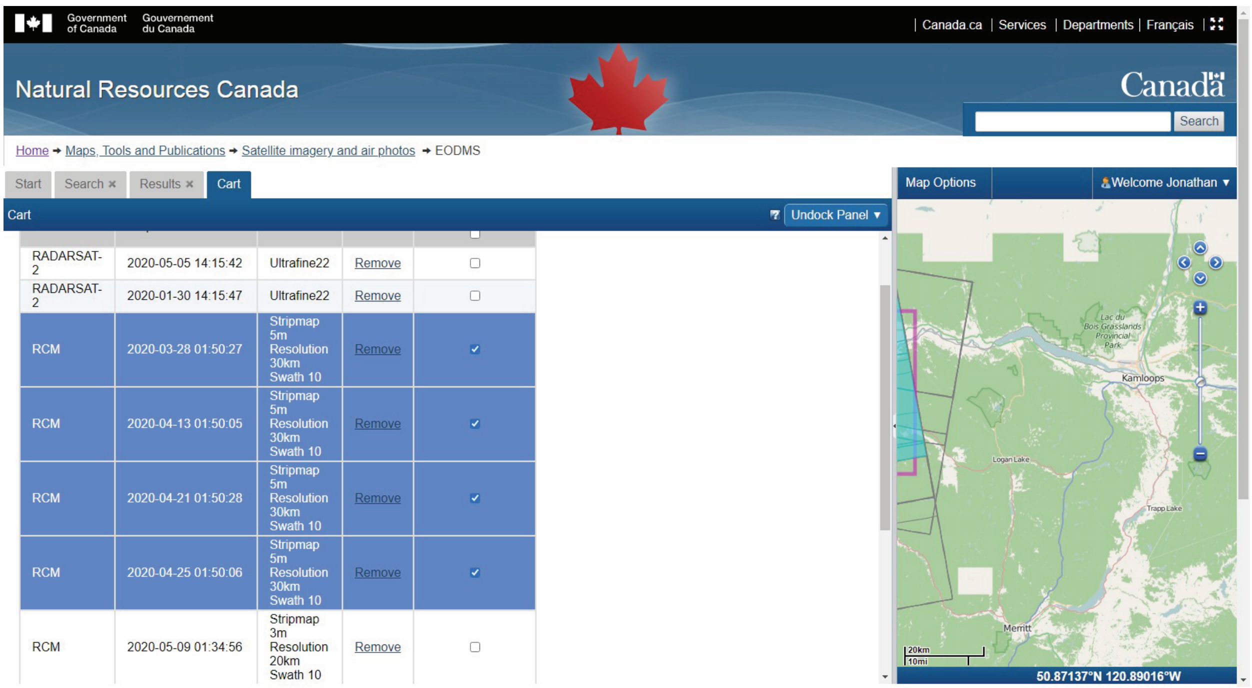

Define Processing Options

Once the images have been selected for processing, the "Define Processing Options for Your Selected Product" button can be selected.

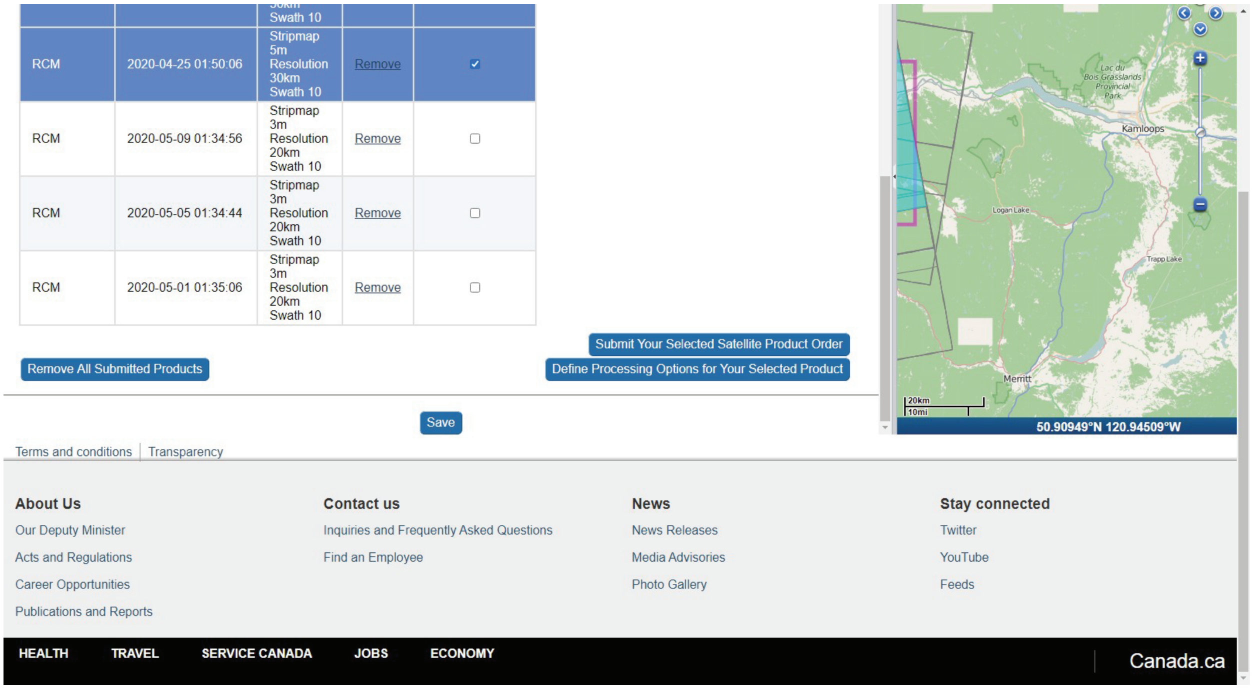

Processing Selected Product List

With the images having been selected for processing, a new "Processing" tab will open. This tab should contain the list of selected image products.

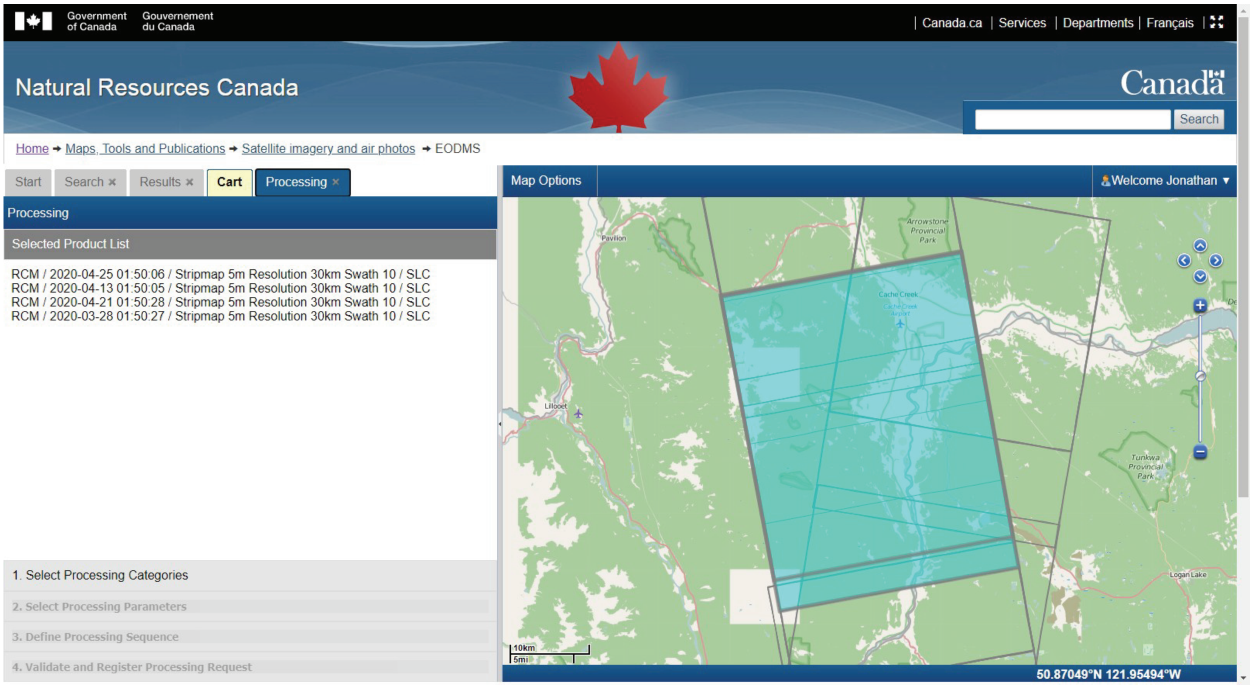

Select Process Categories

Below the "Select Product List" tab is the "Select Processing Categories" tab. Once selected, this tab will display the possible processing options for the SAR data. For DInSAR processing, the "Interferometry" checkbox must be selected. This checkbox cannot be combined with any other processing checkbox.

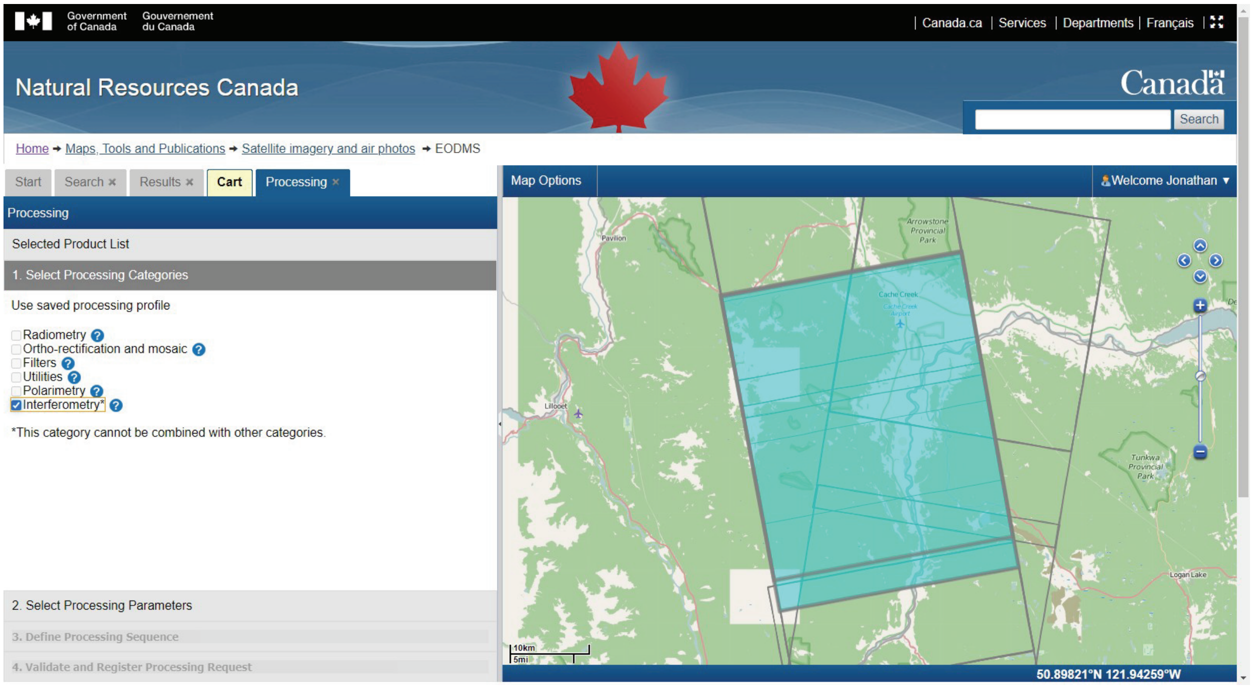

Select Processing Parameters

Once the “Interferometry” checkbox has been selected, the “Select Processing Parameters” tab can be selected. In this tab, the polarization checkbox must be selected. Only **one** polarization can be selected (and cannot be All available) and the polarization must be present in the image data. Next, the processing method can be selected in the Add method dropbox. There are two processing methods: “Ground deformation” and “Very large ground deformation”. The first option (“Ground deformation”) will employ Differential InSAR (DInSAR) processing on the image data. This processing method is suitable if the expected ground movement is approximately a few centimeters or less (between image dates). The second option (“Very large ground deformation”) employs Speckle Offset Tracking (SPO) and is suitable if the expected ground movement is approximately a few meters or more (between image dates).

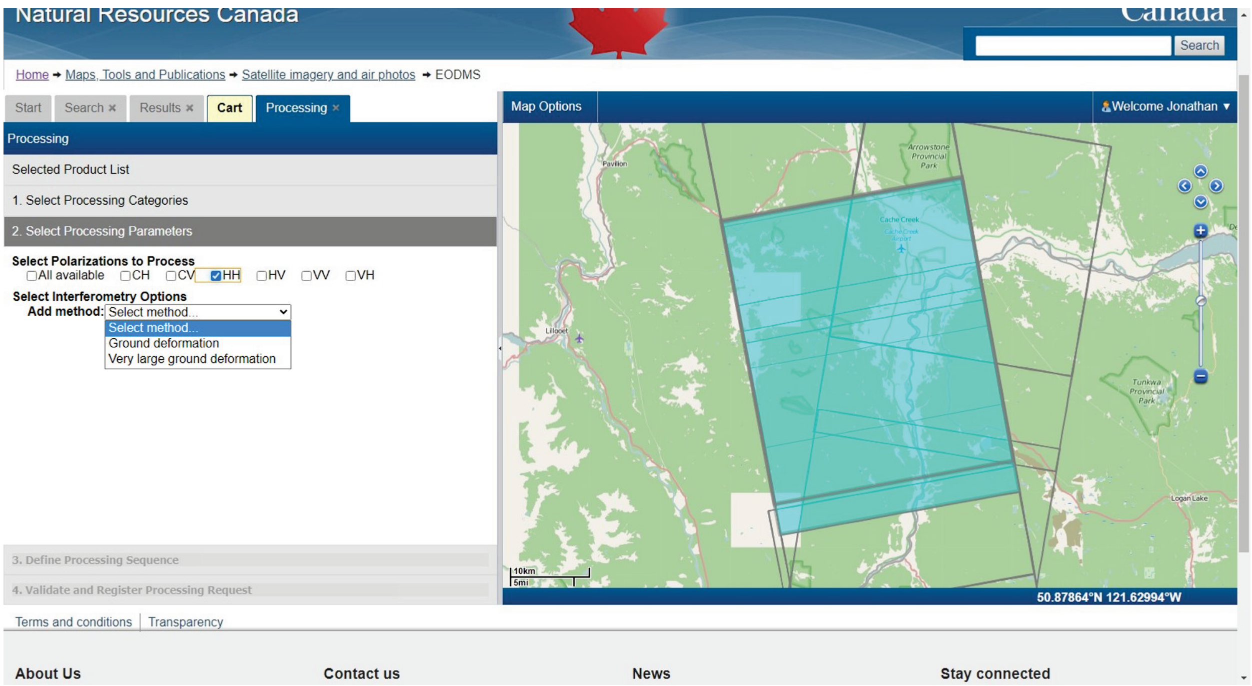

Validation

Once a processing method is selected, EODMS will verify that the input parameter and images for processing. This is done to ensure that the selected polarization is found in the images and that the images are appropriate for DInSAR processing.

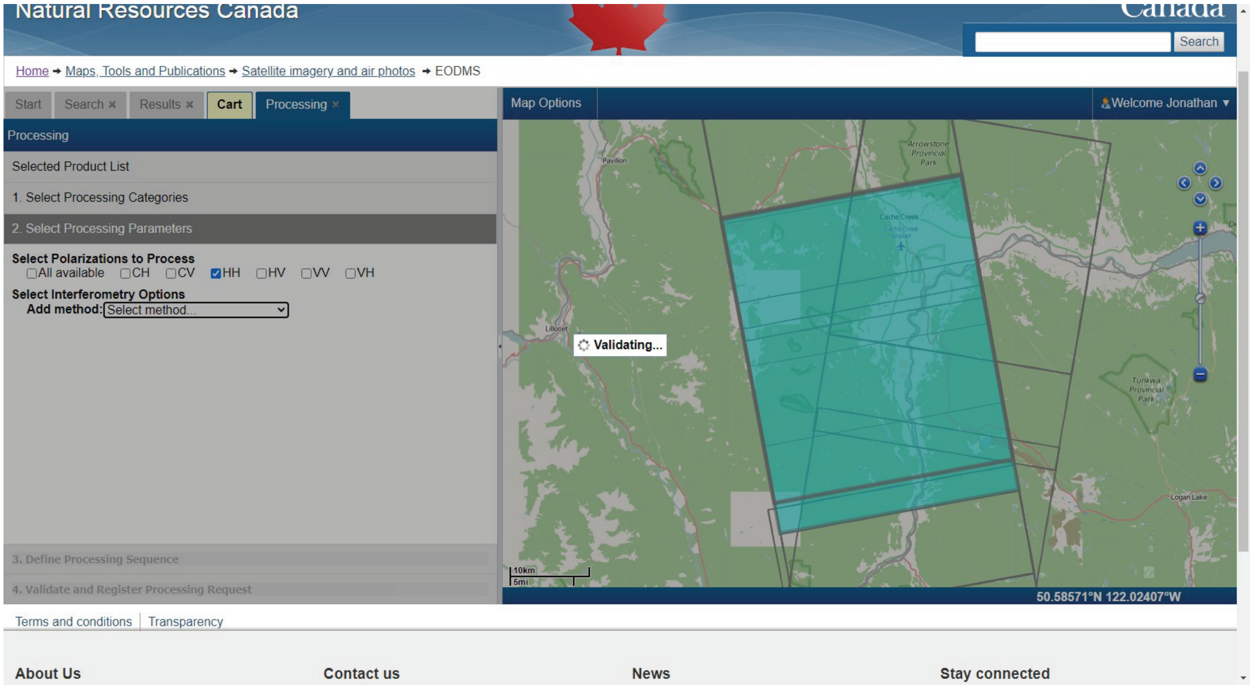

Select Processing Parameters

If validation is successful, the processing parameters for the selected process can be defined. These parameters are used as inputs to the DInSAR system processing algorithm. They include:

- Label name: Name for your processing request
- Master definition: Choose to define a master date to coregister all other images or have it selected automatically by the system
- Spatial averaging: Size of the boxcar filter (multilooking) to apply to the data. This reduces speckle at the cost of resolution. For DInSAR, it is recommended to select the highest multilook which will still preserve the resolution of the expected signal.
- Product enhancement: This parameter controls image enhancement tools such as spatial filtering and coherence limits. It can be set to "Low", "Medium", or "High". In regions with higher coherence, less filtering is required. In regions with lower coherence, more filtering may be beneficial.
- Digital elevation model: Which DEM should be used for the removal of topographic phase. Users can select "CDEM", "CDSM", or "SRTM". The CDSM (20 m ground resolution) covers regions in Canada south of latitude 60°N, CDEM (30 m ground resolution) covers all of Canada, and SRTM (90 m ground resolution) covers the world between latitude 60°S and 60°N.
- Process specific extent: Users can select a subregion within the image for DInSAR processing. This can speed up processing and reduce file sizes if the AOI only spans a small part of the image. If selected, this subregion must also contain stable areas outside of the area undergoing ground movement.
- Output layer options: These define which DInSAR products will be delivered to the user and are listed in the next section.

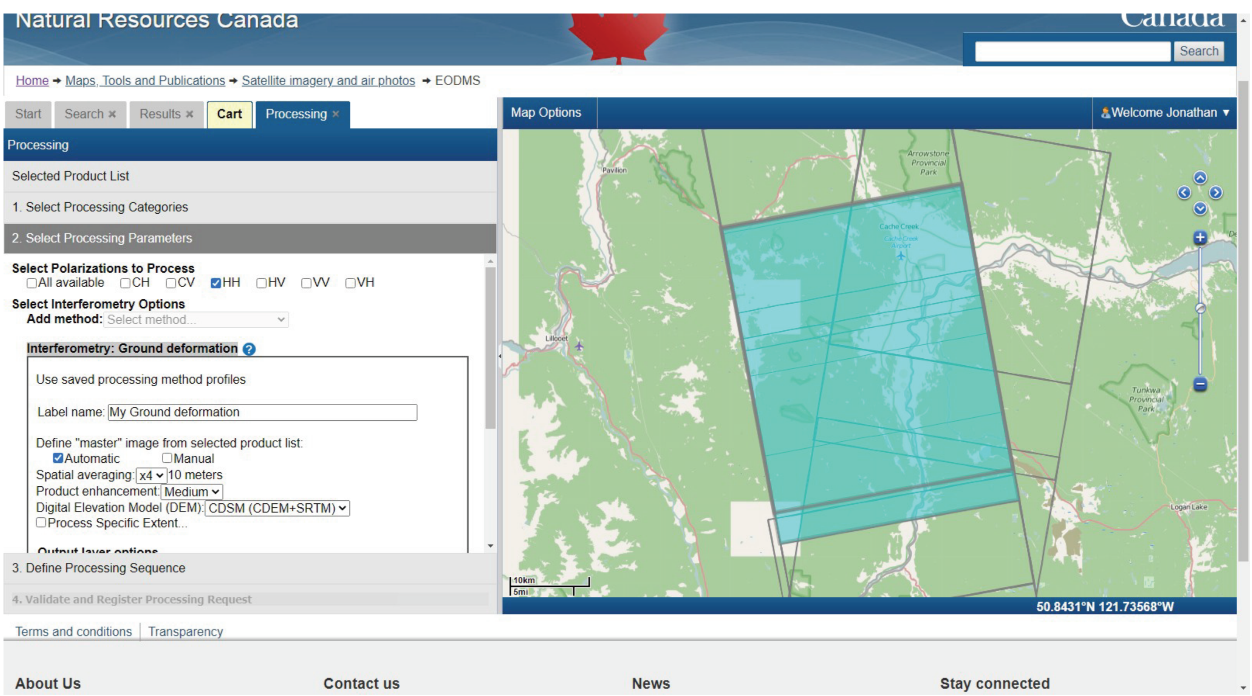

Select Processing Parameters (Ground deformation)

For the “Ground deformation” (DInSAR) processing option the “Output layer options” are all coregistered to the master image date and geocoded. As listed in Table 6 they consist of:

- Digital elevation model: Map of the DEM.
- Coregistered intensity: Intensity images for each image date.
- Coherence: Coherence maps for each interferometric pair.
- Coherence (filtered): Spatially filtered coherence map.
- Wrapped phase: Wrapped phase for each interferometric pair.
- Wrapped phase (filtered): Spatially filtered wrapped phase.
- Unwrapped phase: Unwrapped phase for each interferometric pair.
- Range displacement: Line-of-sight displacement for each interferometric pair.
- Range displacement time series and rate: Continuous, cumulative measurement of the line of sight displacement for each image date. The linear deformation rate is also calculated.

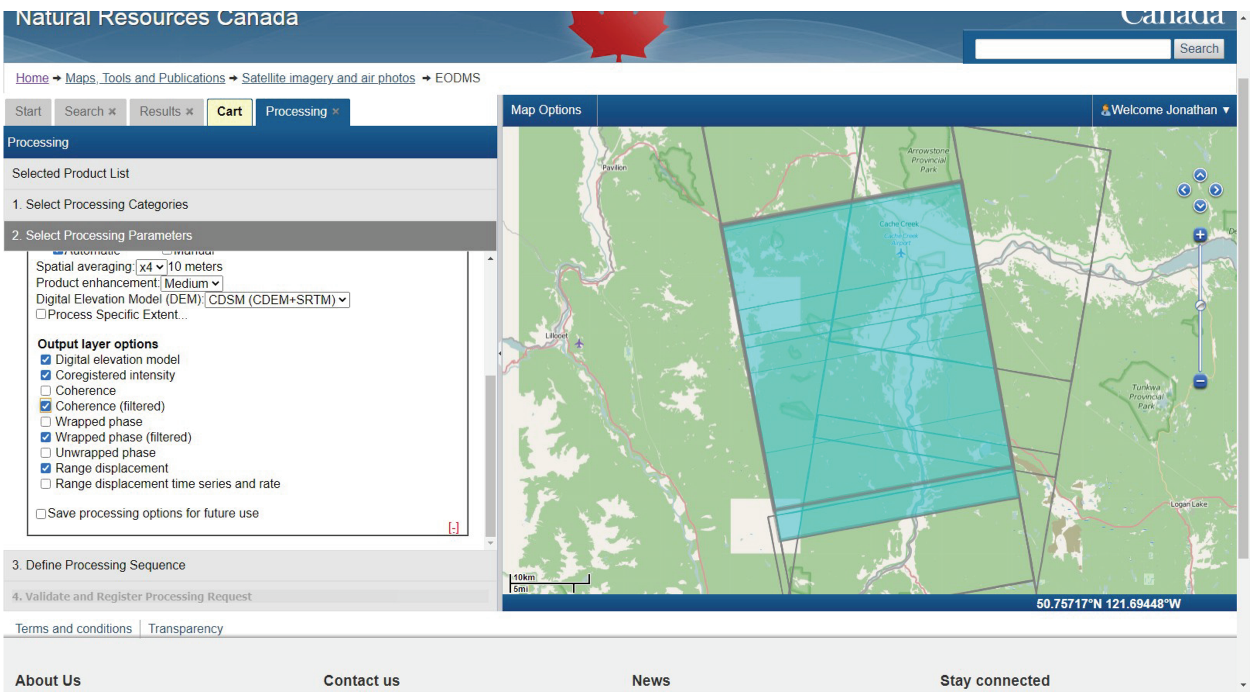

Select Processing Parameters (Very large ground deformation)

For the "Very large ground deformation" (SPO) processing option the "Output layer options" are all coregistered to the master image date and geocoded. As listed in Table 6 they consist of:

- Digital elevation model: Map of the DEM.
- Coregistered intensity: Intensity images for each image date.
- Azimuth/range displacement: Azimuth and range displacement for each interferometric pair.
- Azimuth/range displacement time series and rate: Continuous, cumulative measurement of the azimuth and range displacements for each image date. The linear deformation rates are also calculated.
- 3D displacement (surface parallel flow): East/west, north/south, and up/down displacement for each interferometric pair, assuming that movement follows the local topographic slope.
- 3D displacement time series and rate (surface parallel flow): Continuous, cumulative measurement of the east/west, north/south, and up/down displacements for each image date, assuming that movement follows the local topographic slope. The linear deformation rate is also calculated.

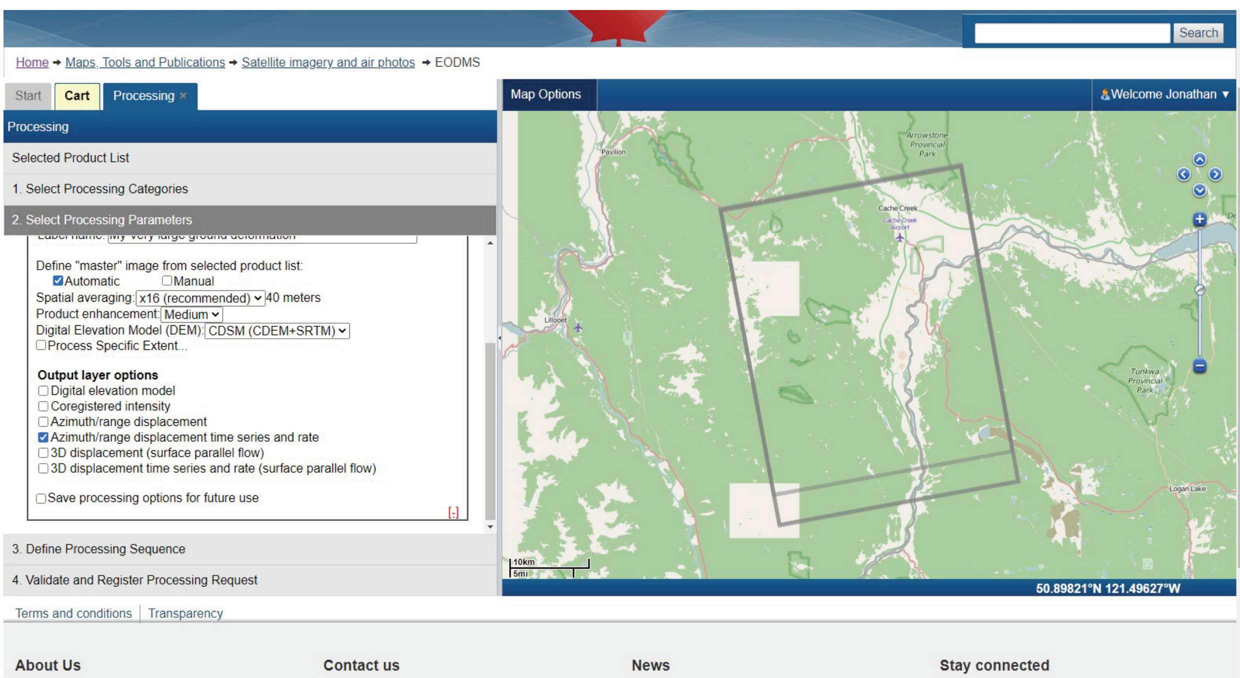

Define Processing Sequence

Once the processing options have been set, the processing sequence can be defined. The method must be selected from the dropbox by its label name and the delivery location must be set. There is also an option to save processing options for future use.

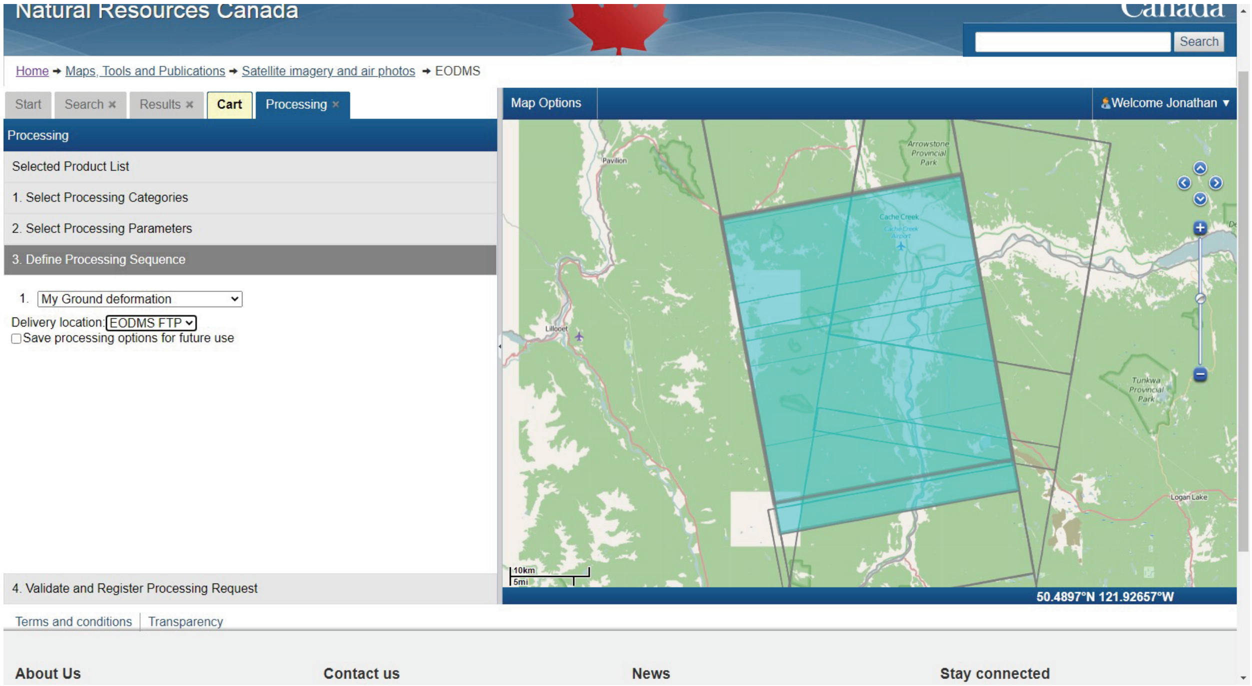

Validate Processing Request

The last step in the process submission is a final validation of the entire request by EODMS. Selecting the "Validate and Register Processing Request" tab reveals the "Validate Processing Request Button". Selecting this button will begin the final validation process.

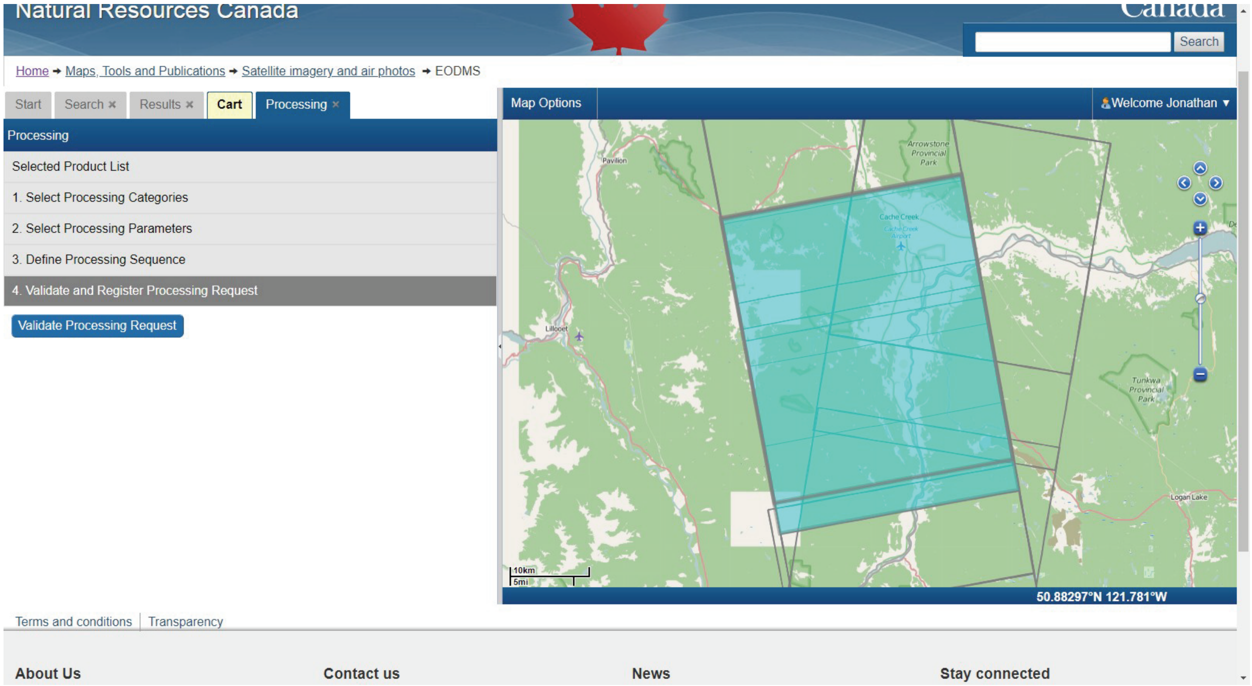

Processing Request Name

Once the validation is complete and successful, the Processing request name can be set and the processing request can be added to the EODMS “Cart” tab.

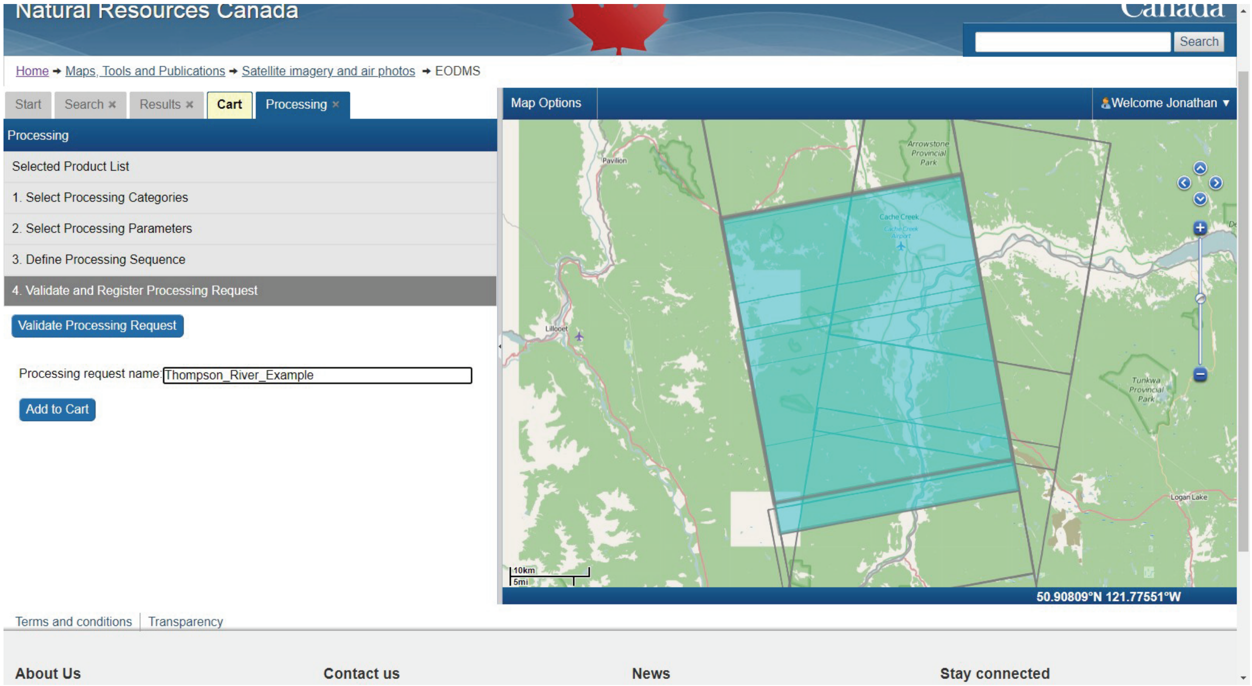

Submit Processing Request Order

From the "Cart" tab the processing request can be submitted to the EODMS VAP system by first selecting the "Request Selection" checkbox for the desired processing request and then selecting the "Submit Your Selected Processing Request Order". This is the final step in the process submission.

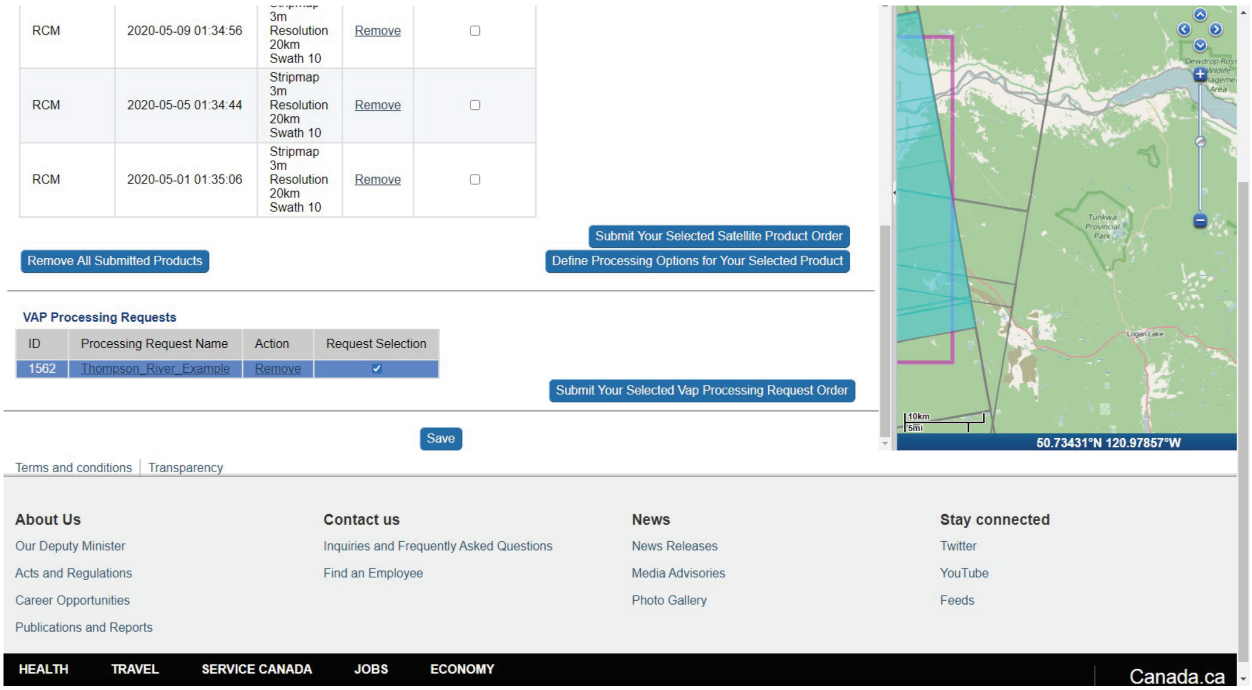

Submit Processing Request Order

Once the order has been submitted, a pop-up from EODMS will verify that it is being sent to the VAP system for DInSAR processing.

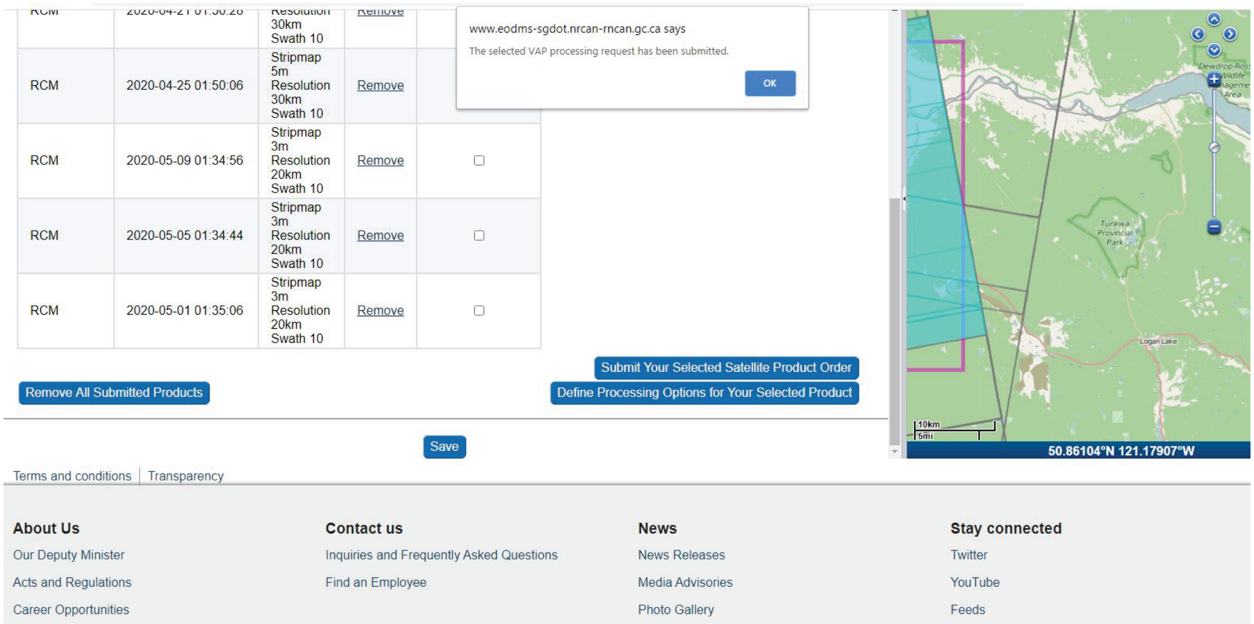

Processing Submitted Notification

As an additional validation of order submission, EODMS will send an email acknowledging the order submission to the VAP system.

EODMS VAP Processing Order Request Submitted Notification

REPLY REPLY ALL FORWARD

nrcan.eodms-sgdot.rncan@canada.ca
Thu 2020-07-02 3:40 PM

Mark as unread

To:

eDOCS | Bing Maps | + Get more apps

Natural Resources Canada | Ressources naturelles Canada | Canada

Dear Jonathan,

Your VAP Processing Order request "Thompson_River_Example"(Order ID: 36001) has been successfully submitted.

You will receive a subsequent notification when the requested processing order has been delivered.

IMPORTANT NOTICE

- If you received this email without having placed a VAP Processing order, please contact the EODMS Support Team.

Thank you and have a nice day,

The EODMS Support Team
nrcan.eodms-sgdot.rncan@canada.ca

Processing Complete Notification

Once the system has processed the request, EODMS will email the user to notify them and to send an HTTP link to where the output data can be downloaded. This signifies the completion of the request.

EODMS VAP Processing Order Request Complete Notification

REPLY   REPLY ALL   FORWARD

nrcan.eodms-sgdot.rncan@canada.ca
Thu 2020-07-02 4:07 PM

Mark as unread

To:

eDOCS | Bing Maps | Action Items | + Get more apps

Natural Resources Canada   Ressources naturelles Canada   Canada

Dear Jonathan,

Your VAP Processing Order request "Thompson_River_Example" (Order ID: 36001) has been processed and is now ready for download at the Earth Observation Data Management System (EODMS) FTP site.

The requested processing order under the account "jdudley" can be found in:

HTTP https://data.eodms-sgdot.nrcan-rncan.gc.ca/public/carts/a70ce489-e2db-49a7-80c6-35a876c0e8e7/141856/bcee340d-5821-4387-aad7-f47bb5551744

IMPORTANT NOTICE

- The above directory and its content will be deleted after 14 days, please download the files before they get deleted.
- If you received this email without having placed a VAP Processing order, please contact the EODMS Support Team.

Thank you and have a nice day,

The EODMS Support Team
nrcan.eodms-sgdot.rncan@canada.ca

Appendix B: Filename Acronyms

adf: adaptive spatial filtering has been applied
bperp: perpendicular baseline
cc: spatial coherence, measured from 0 to 1
ddew: gradient of DEM in east/west direction
ddns gradient of DEM in north/south direction
dem: digital elevation model in meters
disp : line-of-sight displacement in meters
filtered: spatially filtered in SPO processing
geo: georeferenced
kmz: keyhole markup language, zipped
LOS: line-of-sight
lv_phi: horizontal look vector angle in radians
lv_theta: elevation look vector angle in radians
MSBAS: multi-dimensional small baseline subset, cumulative LOS time series measurement in meters
MSBAS_LINEAR_RATE: time series linear rate in meters per year
MSBAS_LINEAR_RATE_R2: coefficient of determination of the time series linear rate
MSBAS_LINEAR_RATE_STD: standard deviation of the time series linear rate
MSBAS_LOG: time series log file
MSBAS_TSOUT: time series parameter file
MSBAS_ZSCORE_MASK: time series z-score
pdf: portable document format
rmli : registered multilook intensity
slc : single look complex
spo: Speckle Offset Tracking
spo_azimuth: azimuth component of displacement in meters
spo_ew: east component of displacement in meters
spo_magnitude: magnitude of displacement in meters
spo_ns: north component of displacement in meters
spo_range: range component of displacement in meters
spo_snr: SPO signal-to-noise
spo_ud: SPO vertical component of displacement in meters
tif: GeoTIFF
ts_azimuth: SPO azimuth time series
ts_3d: SPO 3D time series
ts_insar: DInSAR time series
ts_range : SPO range time series
unw : unwrapped phase in radians
wrp: wrapped phase in radians